NAVAL POSTGRADUATE SCHOOL
Monterey, California

THESIS

DTIC
ELECTE
NOV 02 1992
S E D

A CORRELATION OF
WELDING SOLIDIFICATION PARAMETERS
TO WELD MACROSTRUCTURE

by

FRANCIS G. NOVAK

JUNE 1992

ADVISORS: A.G. FOX
                                 Y. JOSHI

Approved for public release; distribution is unlimited.

REPORT DOCUMENTATION PAGE		Form Approved OMB No. 0704-0188

1a. REPORT SECURITY CLASSIFICATION Unclassified	1b. RESTRICTIVE MARKINGS
2a. SECURITY CLASSIFICATION AUTHORITY	3. DISTRIBUTION AVAILABILITY OF REPORT
2b. DECLASSIFICATION/DOWNGRADING SCHEDULE	Approved for public release; distribution unlimited.

4. PERFORMING ORGANIZATION REPORT NUMBER(S)	5. MONITORING ORGANIZATION REPORT NUMBER(S)

6a. NAME OF PERFORMING ORGANIZATION Naval Postgraduate School	6B OFFICE SYMBOL (If applicable) ME	7a. NAME OF MONITORING ORGANIZATION Naval Postgraduate School
6c. Address (City, State, and ZIP Code) Monterey, CA 93943-5000		7b. ADDRESS (City, State, and ZIP Code) Monterey, CA 93943-5000
8a. NAME OF FUNDING/SPONSORING ORGANIZATION	8b OFFICE SYMBOL (If applicable)	9. PROCUREMENT INSTRUMENT IDENTIFICATION NUMBER

8c. ADDRESS (City, State, and ZIP Code)	10. SOURCE OF FUNDING NUMBERS			
	PROGRAM ELEMENT No.	PROJECT No.	TASK No.	WORK UNIT ACCESSION No.

11. TITLE (Include Security Classification) A Correlation of Welding Solidification Parameters with Weld Macrostructure

12. PERSONAL AUTHOR(S) NOVAK, FRANCIS G.

13a. TYPE OF REPORT Thesis for Master of Science and Mechanical Engineer Degrees	13b. TIME COVERED From: June 1991 To: June 1992	14. DATE OF REPORT (Year, Month,Day) 1992 June 18	15. PAGE COUNT 99

16. SUPPLEMENTARY NOTATION The views expressed in this thesis are those of the author and do not reflect the official policy or position of the Department of Defense or the U. S. Government.

17. COSATI CODES			18. SUBJECT TERMS (Continue on reverse if necessary and identify by block number)
FIELD	GROUP	SUB-GROUP	Welding , Solidification , Solidification Parameters, Weld simulation, Macrostructure

19. ABSTRACT (Continue on reverse if necessary and identify by block number)

A 3-D finite difference model simulating single pass autogenous welds was used to predict the temperature fields in HY-80 steel arc weldments at various powers and torch velocities. From the predicted temperature field, two important solidification parameters were calculated at the solid-liquid interface: temperature gradients and crystal growth velocities. These were correlated with the macrostructures observed in actual weldments. For purposes of model validation, the predicted and actual fusion zone sizes were in agreement, as were the predicted time temperature curves compared to those measured with thermocouples embedded in the plate.

20. DISTRIBUTION/AVAILABILITY OF ABSTRACT ☒UNCLASSIFIED/UNLIMITED ☐ SAME AS RPT. ☐ DTIC USERS	21. ABSTRACT SECURITY CLASSIFICATION Unclassified	
22a. NAME OF RESPONSIBLE INDIVIDUAL Professor Joshi	22b TELEPHONE (Include Area code) (408) 646-3400	22c. OFFICE SYMBOL ME/Ji

DD Form 1473, JUN 86   Previous editions are obsolete.   SECURITY CLASSIFICATION OF THIS PAGE

Unclassified

A Correlation of
Welding Solidification Parameters to
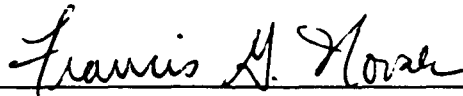Weld Macrostructure

by

Francis G. Novak
Lieutenant, United States Navy
B.S.M.E., United States Naval Academy, 1985

Submitted in partial fulfillment
of the requirements for the degrees of

MASTER OF SCIENCE IN MECHANICAL ENGINEERING
and
MECHANICAL ENGINEER

from the
NAVAL POSTGRADUATE SCHOOL
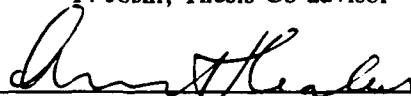June 1992

Author: _____

Francis G. Novak

Approved by: _____
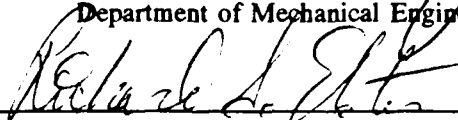
A.G. Fox, Thesis Co-advisor

Approved by: _____

Y. Joshi, Thesis Co-advisor

_____

Anthony J. Healey, Chairman
Department of Mechanical Engineering

_____

Richard S Elster, Dean of Instructions

ii

ABSTRACT

A 3-D finite difference model simulating single pass autogenous welds was used to predict the temperature fields in HY-80 steel arc weldments at various powers and torch velocities. From the predicted temperature field, two important solidification parameters were calculated at the solid-liquid interface: temperature gradients and crystal growth velocities. These were correlated with the macrostructures observed in actual weldments. For purposes of model validation, the predicted and actual fusion zone sizes were in agreement, as were the predicted time temperature curves compared to those measured with thermocouples embedded in the plate.

Accesion For		
NTIS CRA&I		X
DTIC TAB		
Unannounced		☐
Justification		
By		
Distribution /		
Availability Codes		
Dist	Avail and / or Special	
A-1		

DTIC QUALITY INSPECTED 1

TABLE OF CONTENTS

LIST OF TABLES

LIST OF FIGURES

ACKNOWLEDGEMENTS

I. INTRODUCTION

Welding has been the subject of a great deal of research for over four decades. From an engineering standpoint, some of the objectives of the studies include: better prediction and control of weld quality, improved reliability of welds, development of automated welding processes and capability for real time flaw detection. In the case of quality prediction, a lofty ambition would be to provide manufacturers with a system which would calculate material properties of the weld such as strength and toughness based on welding process parameters such as voltage, current, and torch velocity. Or, given strength and toughness specifications, the system would recommend a range of welding process parameters. From a scientific standpoint, the objective is a better understanding of the welding process. A great deal of what physically takes place during welding is still not fully understood.

There are four important zones which are present during the welding of alloys: the fusion zone, the heat effected zone, the mushy zone, and the parent metal. The mushy zone, which exists due to the difference between the solidus and liquidus temperatures of alloys, is the region of finite thickness between the solid heat affected zone and the liquid pool. Many of the important macrostructural characteristics of the weldment are determined in the mushy zone but it is also the mushy zone which is most difficult to study.

The distinction between macrostructure and microstructure is not consistent throughout the literature. By defining macrostructure as those features observable under less than 100X magnification, the macrostructure encompasses the characteristics established during solidification. The microstructure, on the other hand, is determined by the cooling rate of the metal and the characteristics of the continuous cooling rate diagram or, where no phase transformations are involved, by the characteristics of the equilibrium phase diagram. The study of the microstructure involves the subgrain structure.

The important characteristics of the weld are determined in the mushy zone because it is the region where the solidification process occurs. Four parameters, all measured in the mushy zone, affect solidification: temperature gradient, crystal growth velocity, amount of undercooling, and cooling rate. These four parameters establish a solidification mode and consequently, many of the properties of the weld. Detailed discussions of these parameters are provided in various sources.[Ref.1,2,3]

The difficulty in studying the mushy zone of welds arises because it exists only during the welding process. Upon solidification, any region which was the mushy zone is regarded as the fusion zone. To determine the parameters which affect solidification requires making measurements in the weld pool during welding.

Unfortunately, the nature of the welding process renders in situ experiments difficult. The extremely high temperatures lead to problems in measuring the thermal and flow fields of the weldment, which are vital to calculating the solidification parameters. While temperatures have been measured on the surface of weld pools [Ref.4,5], and

2

in spot welds [Ref.6], the temperatures below the surface of a moving weld pool have been elusive. Measurement of temperature curves with embedded thermocouples [Ref.7] and plunged thermocouples (at David Taylor Research Center, Annapolis, Maryland) has been accomplished but with limited success. Empirical data on the important parameters which affect the macrostructure and microstructure of welds is not easily obtainable.

With empirical data pertaining to solidification parameters sparse, computer modeling has come to the forefront in welding research. Ideally, a computer model which simulates the welding process could be likened to a great number of thermocouples and flow measuring devices positioned throughout the weld metal. There is an important shortcoming in computer simulation however. For the same reasons which make it difficult to obtain empirical data in the weld pool, it is equally difficult to validate the models. For the most part, validation techniques are limited to a comparison of computed and actual results while validation of the models in regards to the processes leading to the results is largely speculative. A number of computer models which predict the phenomena of the weld process are constructed elegantly but whether they accurately predict the process is yet to be proven.

Although the validation of a given model may not be entirely conclusive, indications of the model's validity may justify making correlations between calculated and observed results and even cautious predictions of welding results. The conductive heat transfer model of Ule et al [Ref.8,9,10] predicts the three dimensional temperature field in the weld metal. The predicted weld pool penetration sizes have been compared to actual welds, and the temperature profiles under appropriate limiting conditions

3

compared to those of Rosenthal's point source solution. In both cases the agreement between results was reasonable.[Ref.9]

The above model does not account for the effects of undercooling. In a first approximation, the absence of undercooling information can be overcome by confining the study to a single alloy. The effects of undercooling will vary to a large degree from material to material. By correlating the macrostructure of welds of a single alloy to the predicted growth rates and temperature gradients, the effect of welding input parameters is quantified only for the alloy under investigation. By not accounting for undercooling in the calculations, it is required to repeat the entire correlation procedure for any alloy of interest.

II. BACKGROUND

A. LITERATURE SURVEY

1. Thermal Cycles and Rosenthal's Solution

Welding may be described as an intense heat source travelling over a medium. In 1946, Rosenthal presented solutions of the heat diffusion equation for moving point and line heat sources [Ref.11]. An important assumption leading to Rosenthal's solution is that a quasi-steady state exists where the temperature distribution becomes time invariant in a coordinate system moving with the torch. For a heat source moving at velocity v_t, μ is defined as the instantaneous distance from some point of interest to the heat source. The heat source is always at $\mu=0$, the origin of the moving coordinates. Figure 1 illustrates the orientation of the axis and the relationship between the moving and stationary axes.

The differential equation of heat flow in the stationary coordinate system is given by:

$$\nabla^2 \, T = \frac{\partial^2 T}{\partial x'^2} + \frac{\partial^2 T}{\partial y'^2} + \frac{\partial^2 T}{\partial z'^2} = \frac{1}{\alpha} \frac{\partial T}{\partial t'} \qquad \textbf{(1)}$$

where α is the thermal diffusivity. The independent variables are transformed from the fixed to the moving coordinate system in the following manner:

$$x = x' \qquad \textbf{(2)}$$

$$z = z' \qquad \textbf{(3)}$$

$$t = t' \qquad \textbf{(4)}$$

5
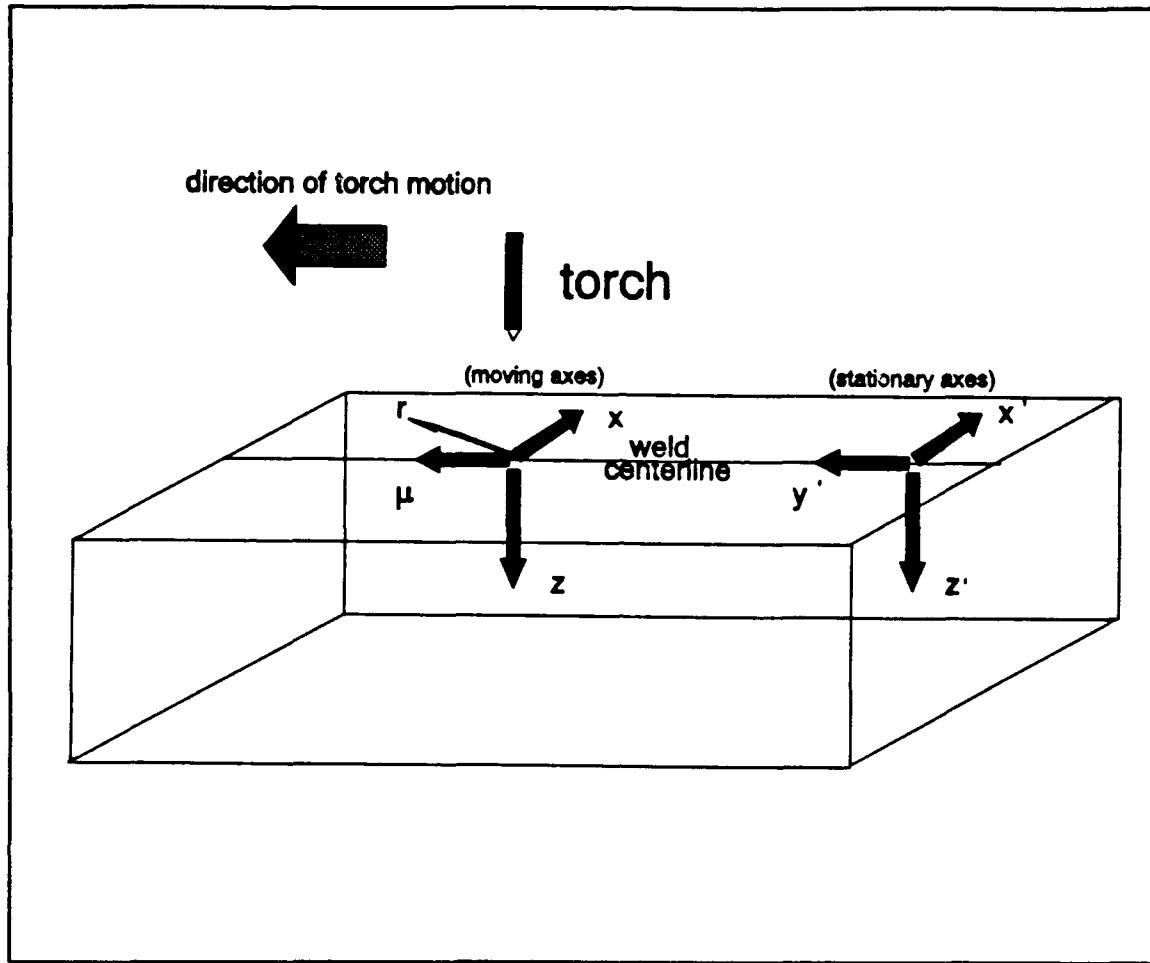
Figure 1 Rosenthal's stationary and moving axes. A quasi-steady state exists in the moving axes.

$$\mu = y' - v_t t' \tag{5}$$

Substituting the transformed variables into equation (1) yields a new form of the equation describing the heat flow:

$$\nabla^2 T = \frac{\partial^2 T}{\partial x^2} + \frac{\partial^2 T}{\partial \mu^2} + \frac{\partial^2 T}{\partial z^2} = \frac{1}{\alpha}\frac{\partial T}{\partial t} - \frac{v_t}{\alpha}\frac{\partial T}{\partial \mu} \tag{6}$$

In the quasi steady state, there is no time dependence in the moving frame. The heat flow equation then reduces to:

$$\nabla^2 \ T = \frac{\partial^2 T}{\partial x^2} + \frac{\partial^2 T}{\partial \mu^2} + \frac{\partial^2 T}{\partial z^2} = - \frac{v_t}{\alpha} \ \frac{\partial T}{\partial \mu} \qquad (7)$$

Rosenthal gave solutions to equation (7) for a number of cases including two important geometric configurations: (1) two dimensional heat flow in a thin plate and (2) three dimensional heat flow in a thick plate. His solutions are in terms of the heat input per unit weld length Q/v_t and the distance from the heat source r:

$$Heat \ input \ per \ unit \ length = Q/v_t = \eta IV/v_t \qquad (8)$$

$$r = (x^2 + \mu^2 + z^2)^{1/2} \qquad (9)$$

where η is the welding efficiency, I is the current, and V the voltage. In the thin plate solution, $z=0$.

Rosenthal's thin plate solution is:

$$T(x,\mu) - T_0 = \frac{Q/v_t}{2\pi k} \exp(-v_t\mu/2\alpha) \ K_0(v_t r/2\alpha) \qquad (10)$$

Rosenthal's solution for the thick plate is:

$$T(x,\mu) - T_0 = \frac{Q/v_t}{2\pi k} \exp(-v_t\mu/2\alpha) \ \frac{\exp(-v_t r/2\alpha)}{r} \qquad (11)$$

where k is the thermal conductivity and in equation (10), K_0 is the zero order Bessel function of the first kind.

Rosenthal's equations are useful for predicting the thermal history at points outside the weld pool. However, for three important reasons, his solutions do not hold in the molten pool. First, the solutions become singular at the heat source location. In

the case of the thin plate solution, the zero order Bessel function goes to infinity as the argument goes to zero; and the distance r appears in the denominator of the thick plate solution. Second, Rosenthal's equations assume constant thermal conductivity and specific heat. Neither of these quantities are constant, particularly above the melting temperature. Finally, his solutions are based only on conduction heat transfer. Fluid motion and convection heat transfer are significant in the weld pool but are not considered. Also, surface radiation is neglected.

The need for thermal history data in the weld pool, without the benefit of an analytical solution, has motivated development of numerical models which predict the thermal and flow fields near and within the molten zone.

2. Numerical Model

Several computational models have been developed to facilitate the study of the fusion zone of welds. This section is an overview of the model of Ule, et al [Ref.10], which is used in the present study.

The model uses finite difference techniques to make three dimensional predictions of the temperature field in weld metal. A semidiscrete technique with explicit time differencing is employed. A fourth order Runge-Kutta algorithm solves the spatial temperature distribution.

Computation times were reduced by creating three distinct grid sizes. The finest mesh moves at appropriate time increments ensuring that the heat source and therefore the steepest temperature gradients, are inside the fine mesh. The fine mesh is nested in a medium mesh, which also moves so that the fine mesh remains within its boundaries. Finally, there is a coarse mesh which houses the medium mesh. The coarse mesh does not move but is large enough that the fine and medium meshes will not leave the coarse mesh even for rather long weld run times.

The construction of three separate grid sizes reduces computation with little loss of accuracy for two important reasons. First, all of the large temperature gradients occur in the fine mesh. As the gradients fall off away from the heat source, the need for

8

fine grid spacing decreases rapidly. Second, since the temperatures outside the fine grid are not extreme, the material properties are treated as constant in the medium and coarse meshes. Holding the material properties constant in the fine zone would be a very non-physical assumption, but keeping them variable in the medium zone would be costly in terms of computation time and of little value in terms of better results.

The heat source is configured using a three dimensional Gaussian distribution. Other heat sources were considered and tested but it was concluded that the Gaussian distribution leads to the most realistic results [Ref.9]. The specific parameters used to configure the heat input distribution as a volumetric or surface distribution are left as variables for the user to set.

The variables which configure the heat source are A1, B1, and C1. These variables control the heat which is applied in the X, Y, and Z directions respectively. Increasing any of these spreads out the heat distribution along the respective axis. For purposes of introducing the heat at node points, the computer model sets the limits of a loop with A1, B1, and C1. For instance, in the X direction, the range of nodes (discrete i values) over which heat is added is established using:

$$i = i_{\text{arc}} \pm (A1/S + constant_1) \qquad \textbf{(12)}$$

where S is the grid spacing. For example, if i_{arc} is 14, S is 1, and $constant_1$ is 2 (all of which are typical values), setting A1=4 would result in heat distribution over discrete i values ranging from 8 to 20:

$$i = 14 \pm (4/1 + 2) = 14 \pm 6 \qquad \textbf{(13)}$$

The variables A1, B1, and C1 also control the rate at which the intensity of heat input falls off along the X, Y, and Z directions. A negative exponential is used to calculate the heat added at a node. The equation is of the form:

$$added\ heat\ =\ constant_2 \cdot e^{-\ constant_3 \cdot (\ XE\ +\ YE\ +\ ZE\ )} \tag{14}$$

where XE, YE, and ZE are based on A1, B1, and C1, respectively. In the case of the X direction for example, the equation used to determine XE is:

$$XE = \left(\frac{(\ i - i_{arc}\ )}{A1} \right)^2 \tag{15}$$

After heat is added at each time step, the model considers conduction heat transfer within the plate. Convection heat transfer in the weld pool is not accounted for directly. However, the Prandtl number in the molten pool is very low ($\approx$ 0.2 for steel). Heat transfer is therefore dominated by conduction. The thermal conductivity of the molten pool is raised to an artificially high value to account for convection heat transfer.

The important calculation made by the model is the time dependent three dimensional temperature field. Time vs. temperature curves for any of the discrete node points are readily available. Furthermore, using a snapshot of the temperature field, temperature profiles along any axis, and contours of temperatures on any surface can be drawn. The availability of these useful results in the weld pool is an important advantage over Rosenthal's solution.

3. Solidification Parameters and the Mushy Zone

Because many of the material properties of welds (and casts) are determined during solidification [Ref.12], recent studies have paid close attention to solidification behavior. Efforts to explain solidification have made use of rapid solidification theory [Ref.13,14], transparent systems [Ref.15,16,17], and mathematical models which predict microscopic features of solidification morphology [Ref.18]. Studies in each of these areas shed light on solidification behavior in welds but truly understanding the solidification of welds inevitably leads to a need to quantify conditions in the mushy zone and correlate these conditions to solidification morphology.

The mushy zone is the region between the molten liquid and the unmelted solid as shown in Figure 2. The temperature in the mushy zone is greater than the solidus temperature but less than the liquidus temperature of the alloy. The fact that the mushy zone exists only during the alloy solidification process makes it difficult to study experimentally. In a transverse section of a solidified weld, the fusion zone, the heat affected zone, and the parent metal are easily observed. During welding, each point in the fusion zone was the mushy zone twice: first during melting and then during solidification.

1- fusion zone
2- mushy zone
3- heat affected zone
4- parent metal
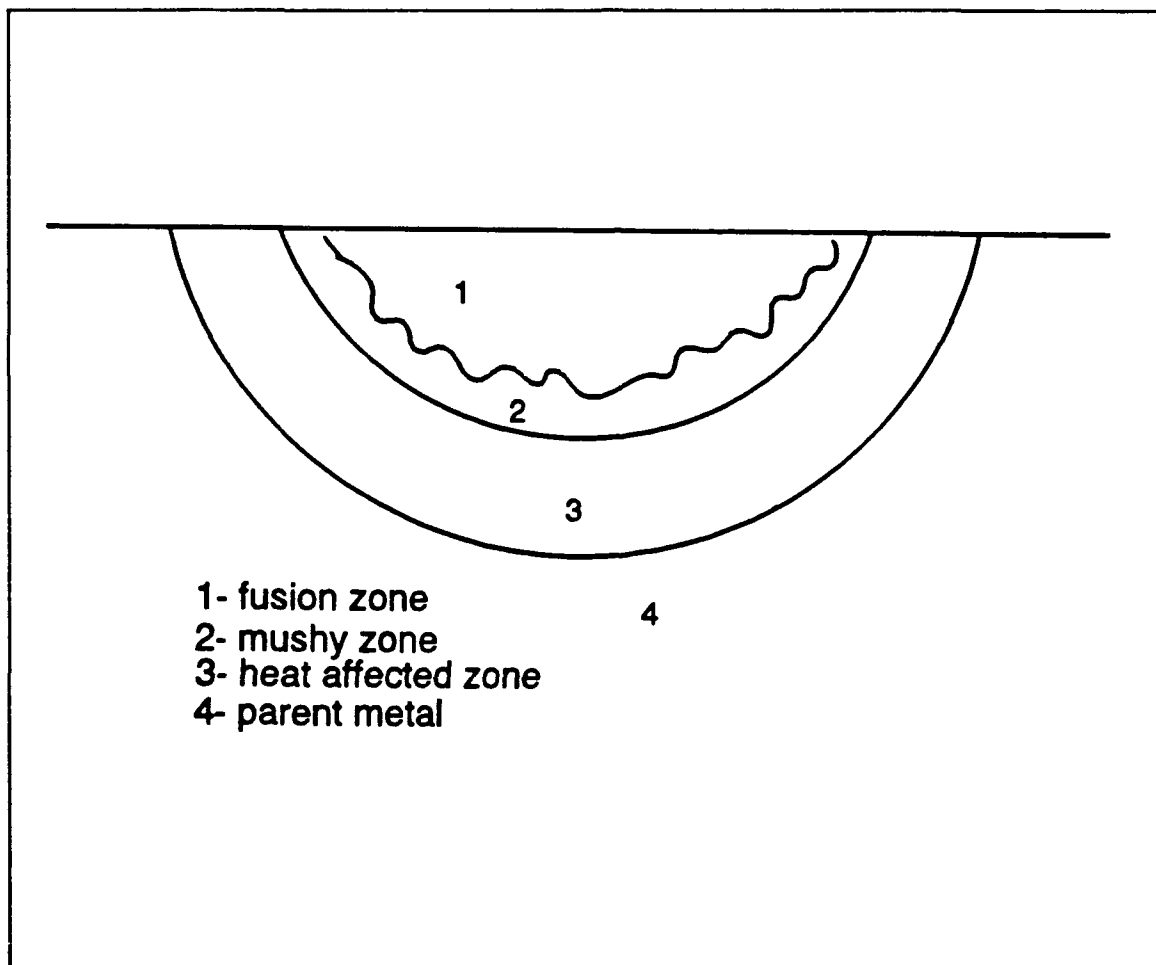
Figure 2 The four zones which exist during the welding of an alloy.

Because solidification takes place in the mushy zone, the mechanical properties can be related to the conditions in the mushy zone which affect solidification behavior. Namely, these conditions are temperature gradient, crystal growth velocity, undercooling, and cooling rate. These conditions will be referred to as solidification parameters in the present study.

The temperature gradient provides the magnitude and direction of the largest change in spatial temperature distribution. Maximum heat flow occurs locally in the direction of the spatial temperature gradient. Considering a point on the solid-liquid interface, two gradients could be calculated: one pointing into the molten pool and the other pointing into the unmelted solid. Since the former affects solidification more directly, it receives a greater amount of attention. In all subsequent references to temperature gradient, the gradient pointing into the liquid pool is implied.

The crystal growth velocity is the rate at which the solid-liquid interface advances. The torch velocity v_t and the weld pool geometry define the crystal growth velocity at all points on the solid-liquid interface if v_t and the weld geometry are assumed to be constant. The crystal growth velocity V is calculated using:

$$V = v_t \cos \theta \tag{16}$$

where θ is the angle between the direction of torch movement and the crystal growth direction as shown in Figure 3.

Undercooling is the difference between the equilibrium liquidus temperature T_E and the actual temperature at the solid-liquid interface. It is the driving force for solidification. Because solute concentration is not constant over the entire solid-liquid interface, the equilibrium liquidus temperature varies locally. The variation of concentration at the interface and the resulting variation in T_E have not been quantified. Therefore, the study of undercooling and its influence on solidification is qualitative.

The cooling rate is the time rate of change of the temperature at the solid-liquid interface. Inspection of a time temperature curve of a point in the weld pool
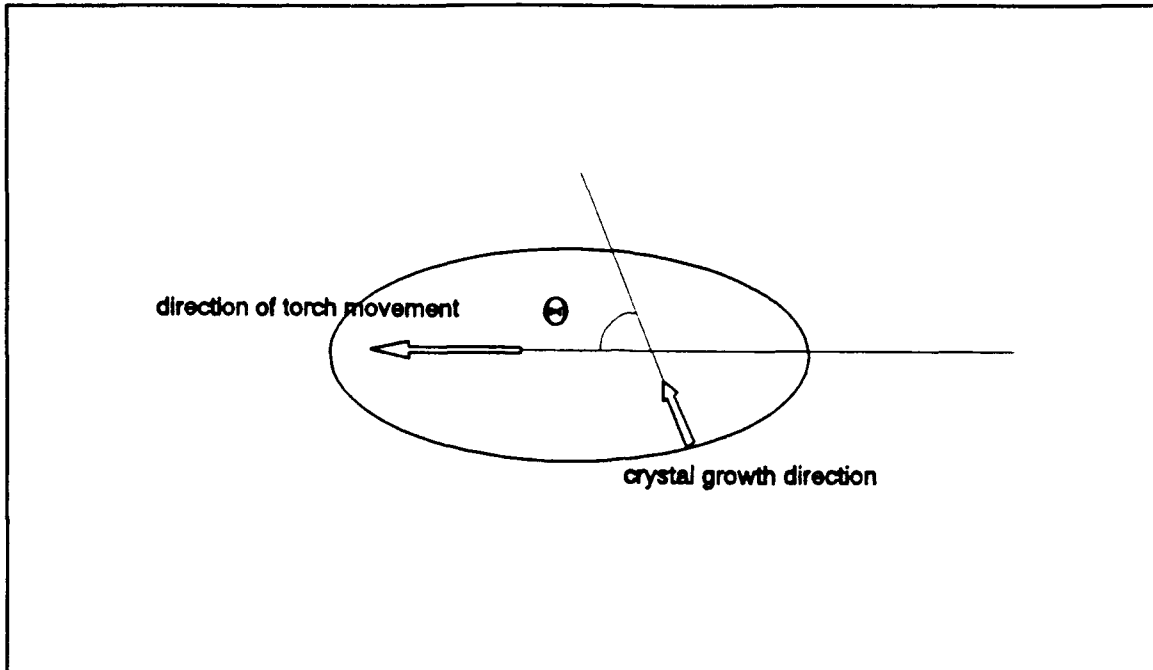
Figure 3 Definition of Θ. A top view of a weld pool. Θ is the angle between the direction of crystal growth and torch movement.

reveals that the cooling rate is not a constant when solidification is occurring. To quantify cooling rate, different methods are employed depending on the application. In some instances, an average cooling rate is calculated which accounts for all of the cooling rates experienced during solidification. A similar approach involves a calculation of the elapsed solidification time. Perhaps the most common way the cooling rate is calculated is by simply taking the product of the temperature gradient at the solid-liquid interface and crystal growth velocity.

4. Solidification Morphology

The solidification of a weldment is governed by the parameters listed above: temperature gradient G, crystal growth velocity V, undercooling, and cooling rate. The solidification morphology is governed by the ratio G/V and the scale is influenced by the product GV (the cooling rate) [Ref.12]. Being able to calculate the parameters G and V and correlate them to the solidification morphology will lead to a better understanding of solidification behavior during the welding process [Ref.1].

13

In a weldpool, G and V vary by orders of magnitude. It is known that the crystal growth velocity is maximum where the temperature gradient is minimum and vice versa, as shown in Figure 4. The crystal growth velocities will be smallest at the extreme edges of the fusion line where the angle Θ between the crystal growth velocity and the heat source velocity is nearly 90°. In contrast, along the weld centerline at the surface of the weld pool, the velocity is greatest because the angle approaches zero. It follows that the temperature gradient is maximum at the fusion line and minimum at the centerline.[Ref.1,2]
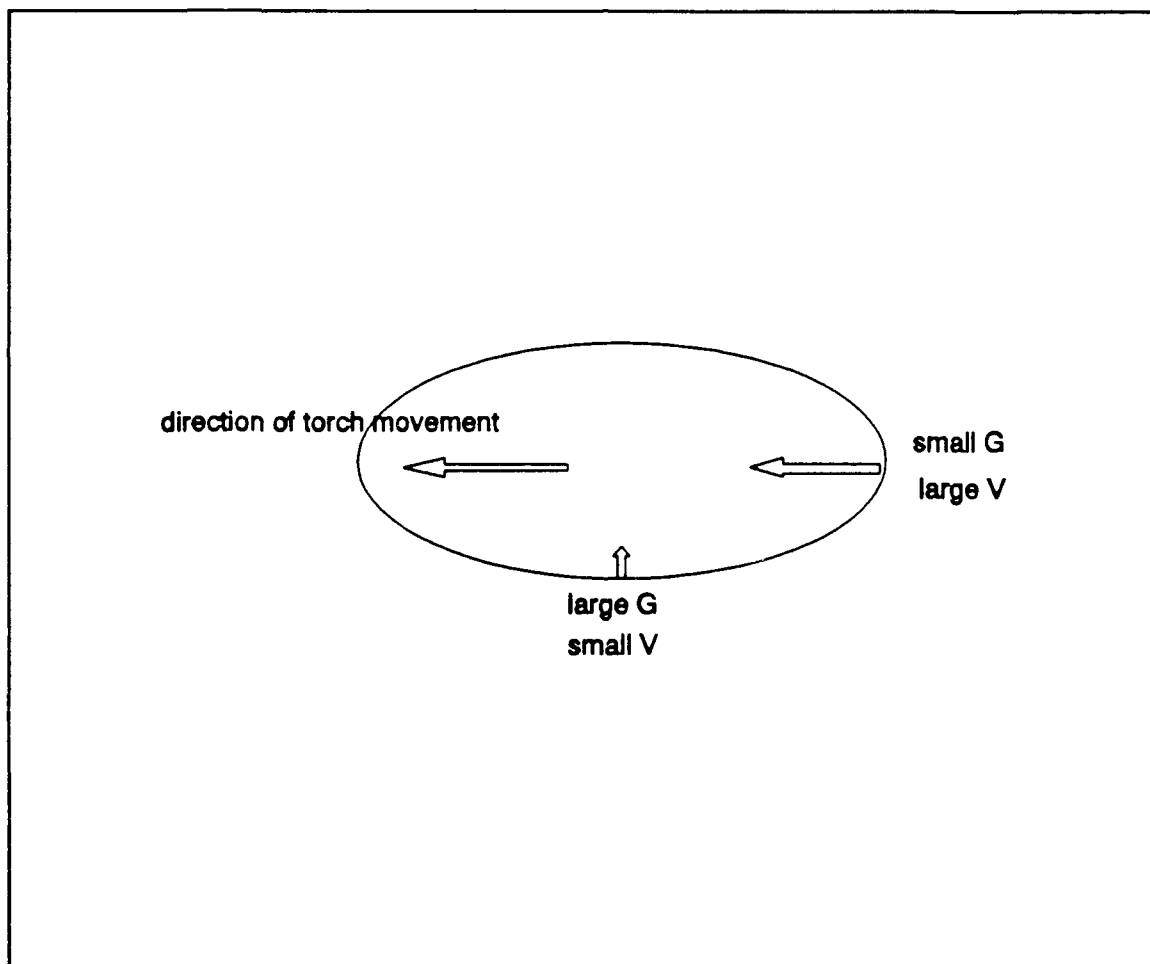
Figure 4 Variation of the temperature gradient G and crystal growth velocity V in a weld pool.

Because of these large fluctuations in G and V in the weld pool, significant variations in the solidification morphology are observable in a single weld pool cross section. In this report, the solidification morphology will be treated on two levels: the macrostructure and the substructure. The macrostructure, which is viewed easily at magnifications of 10X, consists of equiaxed crystals and columnar crystals, as seen in Figure 5. Columnar crystals are distinguishable from equiaxed crystals in that they are longer and share a parallel axis. Whether equiaxed or columnar, the size of the crystals may vary considerably in different weldments or even in one weldment.

The solidification substructure, generally viewable at magnifications of 100X, encompasses the different structures which result from changes in solidification modes. The solidification modes include planar, cellular, columnar, and dendritic, as illustrated in Figure 6. It is noteworthy that various sources may treat the solidification modes differently. In particular, columnar and dendritic are often treated as a single solidification mode.

B.   INFLUENCE OF SOLIDIFICATION PARAMETERS ON MORPHOLOGY

1.   Macrostructure

Lower crystal growth velocity favors an equiaxed crystal macrostructure while a higher velocity results in columnar crystals. As torch speed is increased, the crystal growth velocity increases, and therefore, a need for more directional solidification arises. When the torch velocity is high, long columnar crystals may form which extend from the solid-liquid interface toward the heat source (center of the weld pool).

The temperature gradient also is important in the development of the macrostructure. Lower gradients tend to favor columnar crystals while higher gradients lead to equiaxed crystals.

The combination of lowest gradients and highest velocity, leading to a minimum G/V, occurs at the weld centerline. Very long columnar crystals parallel to the torch velocity sometimes are observed at the weld centerline. Columns which originate near the fusion line often bend toward the torch axis as they grow to the center of the

15
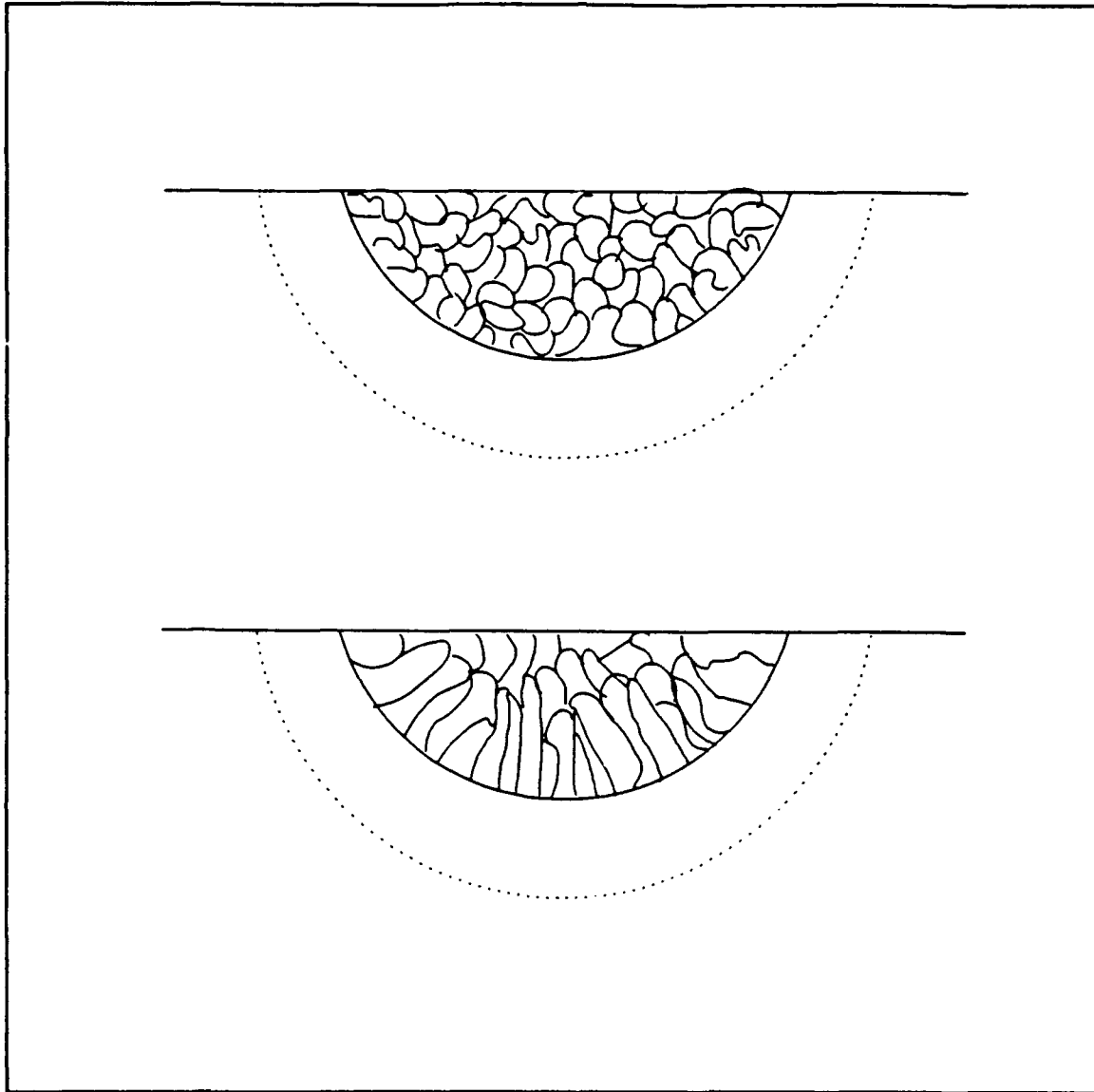
Figure 5 Macrostructures observed in a weldment.

fusion zone. On the other hand, the highest gradient and lowest velocity, the maximum G/V occurs at the fusion line. There is a layer of planar growth at the fusion line. Just inside the fusion line, the macrostructure is likely to be equiaxed crystals.

2. Substructure

As the solid-liquid interface of an alloy advances, solute is rejected into the liquid, causing a high concentration of solute on the liquid side of the interface. The

16
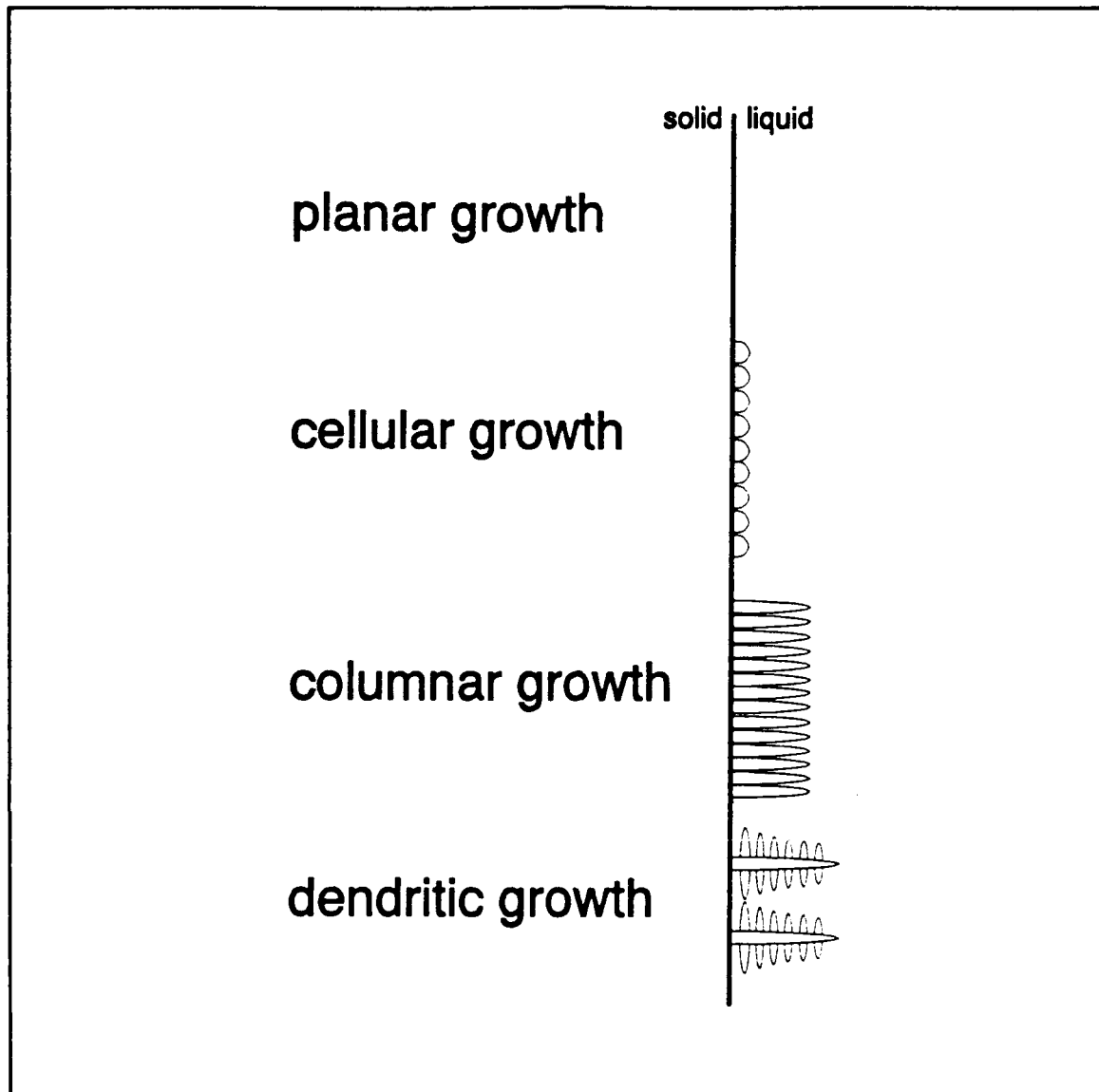
Figure 6 Substructures observed in a weldment.

variation of concentration with distance from the solid-liquid interface is given qualitatively in Figure 7a. Moving away from the interface, the concentration drops off and in liquid far from the interface, the concentration remains nearly that of the overall composition of the alloy. Since the liquidus temperature varies with concentration, as shown in Figure 7b, the liquidus temperature varies with distance from the solid-liquid interface.

17
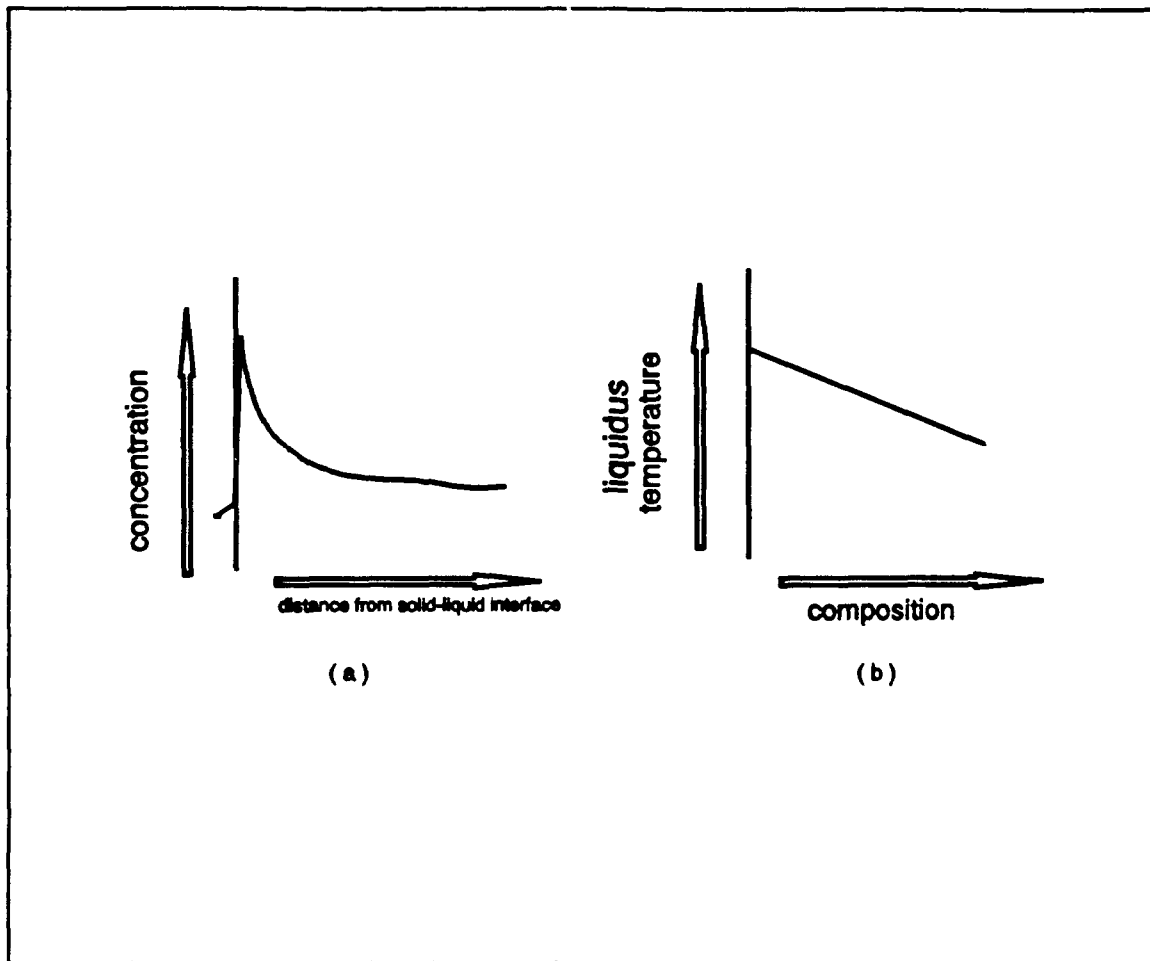
Figure 7 Nonequilibrium conditions at the solid-liquid interface. The variation of (a) concentration with distance from the solid-liquid interface; and (b) equilibrium liquidus temperature with concentration.

If the alloy concentration distribution with the distance from the solid-liquid interface were known, a curve of equilibrium liquidus temperatures T_E could be drawn. The relationship between the slope of the T_E curve to that of the actual temperature gradient, G, at the interface is extremely important. When G is greater than or equal to the slope of T_E at the interface, the solidification mode will be planar. However, when G is less than the slope of T_E, the condition called constitutional undercooling is present and the solidification mode changes.

18

The solidification modes active under the condition of constitutional undercooling lead to cellular, columnar, or dendritic substructures. The condition of constitutional undercooling is illustrated in Figure 8.
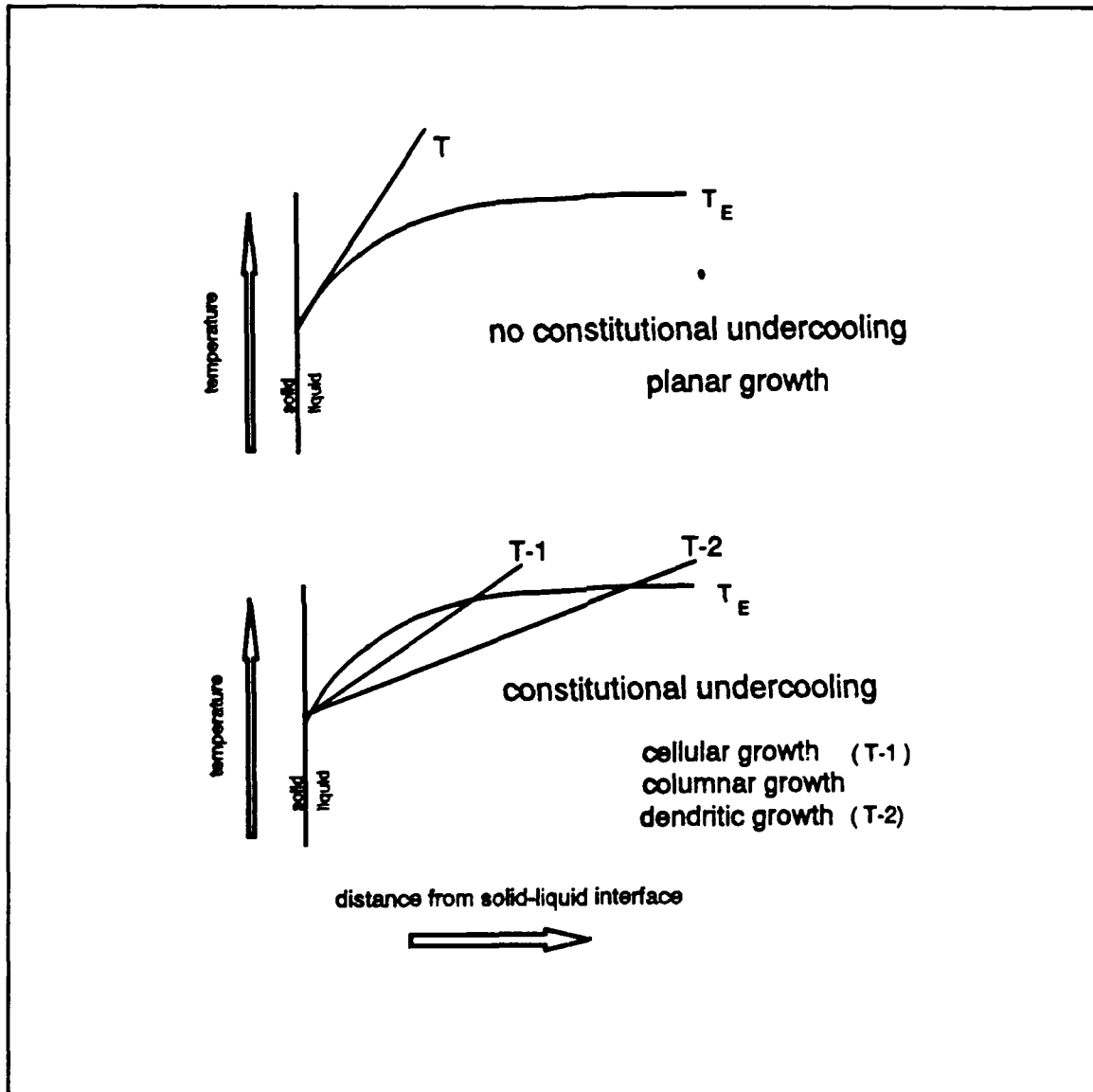
Figure 8 Constitutional undercooling. When the temperature gradient is less than the slope of the equilibrium liquidus temperature curve at the interface, constitutional undercooling is present.

The solidification mode cannot be classified by the temperature gradient alone. The influence of crystal growth velocity also must be considered, as shown in Figure 9. When the velocity is very low, solute rejection is minimal and the solidification mode will be planar. As the velocity is increased, there is a transition velocity at which the solidification mode abruptly changes to cellular. As the velocity is further increased, the solidification mode changes, but not abruptly, to columnar, then dendritic. Finally, if the velocity is increased beyond the limit of absolute stability, there is insufficient time for solute rejection and the solidification mode is again planar.[Ref.15]
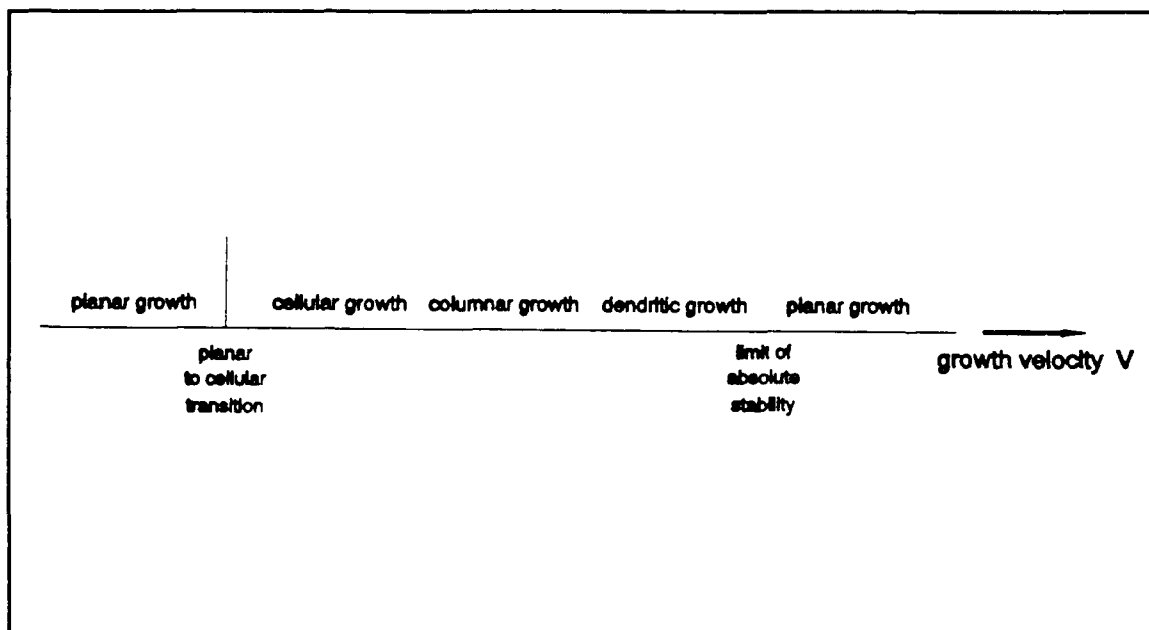
Figure 9 The relationship between the crystal growth velocity V and the solidification mode.

3. Correlations

The importance of predicting and controlling the performance of welds has been the motivation for numerous correlations. The evolution of the correlations is tied closely to the development of the understanding of the welding process. Understandably, early correlations were comparisons between some input variables such as estimated heat input to specific material properties of the weld. Recent correlations relate specific

welding solidification parameters to macrostructural or microstructural features of weld morphology. Then, morphology is related to mechanical properties. Modern correlations have the advantage that they are a window to understanding solidification behavior. Through an understanding of solidification behavior, the material properties may be predicted or controlled.

a. Correlations using Crystal Growth Rate

The solidification parameters have been correlated with solidification morphology in numerous ways. In particular, the growth rate has been used extensively. The following is a summary of some of the correlations using crystal growth rate and the important conclusion.

- Percent of dendritic structure on the weld surface [Ref.2]; For stainless steels, as the growth rate is increased, the structure is dominated more by equiaxed dendritic solidification.

- Weld pool shape [Ref.1]; When growth rate increases with torch velocity, the weld pool shape (free surface shape) goes from elliptical to tear drop.

- Dendrite tip radius [Ref.18]; Generally, the radius decreases with increasing velocity until, at some high velocity, the radius becomes very large. When the radius becomes very large, the solidification mode has changed back to planar at the limit of absolute stability. The tip radius is predicted by a model for a range of growth velocities.

- Dendrite trunk spacing [Ref.1]; The trunk spacing does not vary as greatly as the tip radius. The important relation is that between the tip radius and the spacing because together, they define the dendrite geometry. When the growth rate is high, the tip radius is small compared to the trunk spacing. The result is a needle like dendritic structure. At lower growth rates, the radius is greater than the spacing, leading to cellular or even planar structure. Again, the trunk spacing is predicted by a model for a range of velocities.

- Dendrite tip temperature [Ref.1,18]; and dendrite composition [Ref.1]; The conditions at the dendrite tip dictate whether the conditions for constitutional

undercooling are satisfied and if so, to what extent. In these correlations the growth velocities are predicted by models based on a range of temperatures and compositions. Actual undercooling would be a difficult quantity to measure empirically. There presently are no means to measure the temperature at the tip of a dendrite. This correlation is based on an analytic solution.

- Partition coefficient [Ref.1]; At high growth rates, less solute segregation takes place and the solidified structure is more uniform in composition. Solute segregation is extremely difficult to measure with confidence. The correlation presented is the prediction of partition coefficient for a range of velocities.

b.   Correlations Using Cooling Rate

The cooling rate is also used in a number of correlations, some of which are presented here.

- Dendrite arm spacing [Ref.3]; The dendrite arm spacing decreases with increasing cooling rate. This result is in agreement with the notion that higher cooling rates result in a finer scale substructure.

- Secondary dendrite arm spacing [Ref.1]; The secondary dendrite arm spacing also decreases with higher cooling rates. An average local cooling rate is used and the spacing is measured.

- Percent ferrite [Ref.1]; It was shown that the amount of ferrite in laser welded stainless steels increases with cooling rates. This trend is attributed to the high cooling rates preventing the transformation of primary ferrite to austenite. Percent ferrite is measured in laser welds, and the cooling rate is estimated.

c.   Other Correlations

There are instances where other parameters are correlated with solidification morphology. The parameter $(q/V)^{1/2}$ (where q is the heat input, and V the weld volume), referred to as the solidification parameter by David and Vitek [Ref.1], is correlated with dendrite arm spacing. The greater the solidification parameter, the coarser the dendrites. The heat input P/V_t (P is power, V_t the torch velocity) also is correlated with the dendrite arm spacing. The dendrite arm spacing increases with heat

input. Neither the $(q/V)^{1/2}$ nor the P/V_t correlations address the significant variations of the dendrite arm spacing within the weld pool.

Savage et al studied the relationship between cell size and growth rate as well as cell size and inverse of the temperature gradient pointing into the solid, G_s for very thin plates [Ref.19]. The diameter of the cells decreased with growth rate and increased with $1/G_s$.

4. Qualitative Correlation of G and V with Morphology

G and V are used extensively in models which predict specific features of the morphology. However, although the temperature gradient and crystal growth velocity govern the solidification morphology, correlations which quantify the relationship are noticeably absent.

To qualitatively describe the relationship between the weld macrostructure with the temperature gradients and crystal growth velocities, a log-log plot with the temperature gradient on the horizontal axis and velocity on the vertical axis has been used. This type of diagram first appeared in [Ref.12] but was relevant to casting as it was presented. A similar diagram appeared in [Ref.1] and reflected a modification of Easterling which made the diagram germane to welding.

Taking data points (G,V) at the fusion line and moving toward the pool center, the path will appear as shown in Figure 10. Diagonals leading from the lower left to upper right are lines of constant G/V. High values of G/V would lead to a planar solidification mode. Lower values for G/V indicate that constitutional undercooling is present. The lower the value of G/V, the greater the degree of undercooling.

The important conclusions which can be drawn from this trend are:

1. An equiaxed crystal macrostructure and planar substructure are most likely to occur near the fusion line.

2. Columnar macrostructure and a dendritic substructure will most likely exist at the weld centerline.
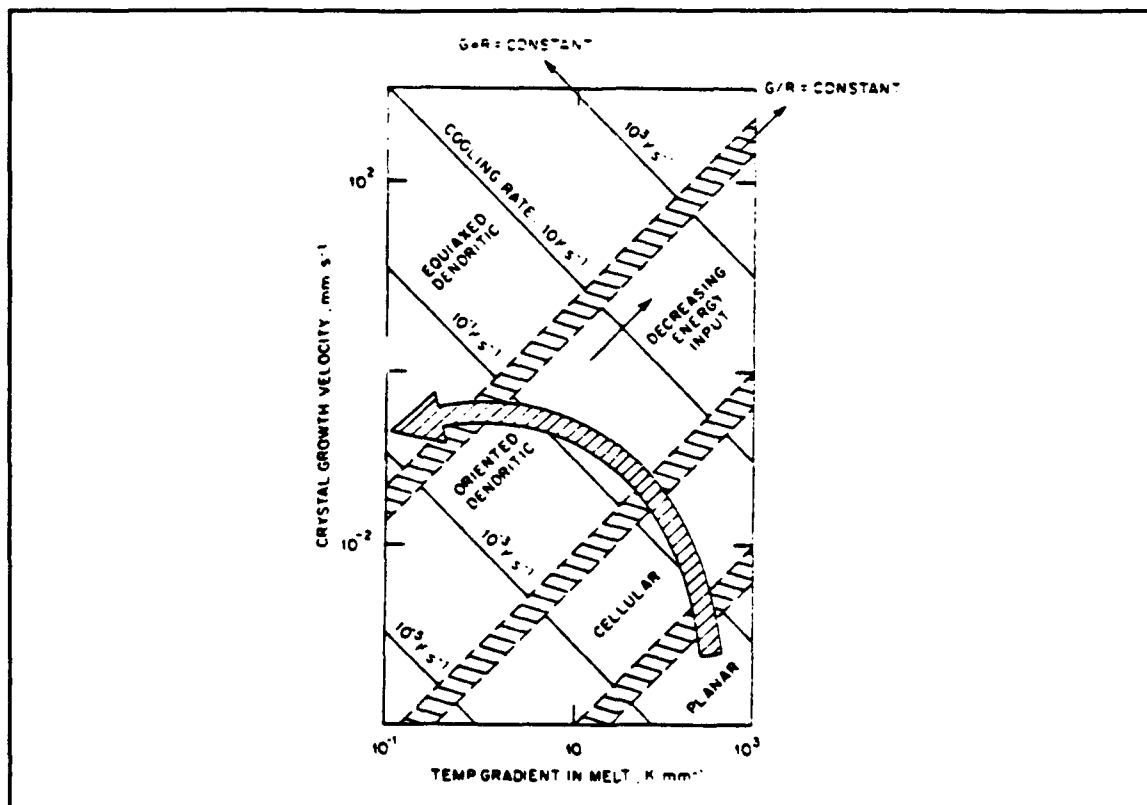
Figure 10 GV type plot presented by David and Vitek [Ref.1].

Diagonals from lower right to upper left are lines of constant GV, or cooling rate. The greater the GV product, the finer the morphology.

Despite the useful insight gained from the GV plot presented here, it is only a qualitative tool. It has not been used to understand the solidification behavior of actual welds.

C. SCOPE OF THE PRESENT WORK

It is evident from the preceding sections that a need exists to quantify the solidification parameters for a subsequent correlation to solidification behavior. It is proposed that the GV Plot can be used for quantitative correlation of the solidification parameters G and V with the solidification morphology. The values for G and V will be calculated using the temperature field predicted using the finite difference model and correlated with the morphology observed on actual weldments.

24

1. Calculating Temperature Gradient and Growth Velocity

a. *Assumptions*

In order to calculate the gradients and velocities based on the predicted temperature field, three important simplifying assumptions must be made. First, the quasi-steady weld pool size and shape are constant. Second, the crystal growth velocity is locally normal to the solid-liquid interface. Finally, the solid-liquid interface is an isothermal surface.

Each of these assumptions is necessary and together, they are sufficient for the calculation of G and V using a 3-D temperature field and the torch velocity. The constant weld pool geometry enables the calculation of growth velocity using only the torch velocity and the angle between the crystal growth and torch velocity. When the solid-liquid interface temperature is constant, the temperature gradient is the normal derivative. Thus, the crystal growth velocity is everywhere parallel to the gradient under the second assumption. The components of the gradient may be used to calculate the direction of velocity.

Each of the three assumptions is a simplification of the real physical nature of welding. The weld pool size and shape are not constant. Rather, time dependent variations in weld pool geometry have been confirmed [Ref.20,21]. The crystal growth velocity will tend to be along preferred [100] growth directions rather than normal to the solid-liquid interface. The solidification direction will change between the [100] directions as these directions become more aligned with the temperature gradient. The velocity will increase or decrease as necessary so that the solid-liquid interface will keep pace with the torch. Finally, the solid-liquid interface is not an isothermal surface. As solute is rejected into the liquid, the solidus and liquidus temperatures will change with concentration.

Despite the simplifications introduced by the assumptions, for the purposes of the present study, the damage is not severe. The time averaged weld pool geometry is constant and the average velocity should be nearly normal to the solid-liquid

interface. As for the isothermal nature of the interface, there does not exist a means to correct for solute rejection which would ensure a better approximation of the surface.

b. Calculations

To accomplish the calculations, the model of Ule et al [Ref.10] will be utilized. The 3-D model provides a temperature field around the heat source. In this temperature field, all four of the regions are present: molten, mushy, heat affected, and parent. The solid-liquid interface of the weld, which is assumed to approximate the mushy zone, is found by locating the isothermal surface which corresponds to the melting temperature of the metal.

The velocity of the interface will be calculated using the equation:

$$V = v_t \cos \theta \tag{17}$$

where V is the magnitude of the crystal growth velocity, v_t is the magnitude of the heat source velocity, and θ is the angle between the two velocity vectors (see Figure 3).

The temperature gradients on the solid-liquid interface will be calculated using a Taylor series expansion about a point X,Y,Z on the surface. Neglecting higher order terms, the general equation is of the form:

$$T(X+\delta X, Y+\delta Y, Z+\delta Z) = T(X,Y,Z) + T_X \delta X + T_Y \delta Y + T_Z \delta Z \tag{18}$$

In this equation, the two temperatures and the three distances are known and the three partial derivatives are unknown. To solve for the partial derivatives, two additional points in the vicinity of (X,Y,Z) and in the weld pool will be selected and used to construct equations similar to equation (18):

$$T(X+\delta X, Y, Z+\delta Z) = T(X,Y,Z) + T_X \delta X + T_Z \delta Z \tag{19}$$

$$T(X, Y+\delta Y, Z+\delta Z) = T(X, Y, Z) + T_Y \, \delta Y + T_Z \, \delta Z \qquad (20)$$

By simultaneously solving equations (18)-(20), T_X, T_Y, and T_Z can be determined.

As stated above, under the assumption that the interface is isothermal, the gradient is the normal derivative. Therefore, the following holds:

$$T_{\hat{n}} = \nabla T = \hat{i} \, T_X + \hat{j} \, T_Y + \hat{K} \, T_Z \qquad (21)$$

Furthermore, the velocity is parallel to the normal derivative which is the gradient. Therefore, $\cos \Theta$ of equation (17) can be calculated using components of the gradient. Since the geometry of the model is such that the heat source velocity is along the Y-axis, $\cos \Theta$ may be calculated using the Y component of the temperature gradient:

$$\cos\theta = \frac{T_Y}{|\nabla T|} \qquad (22)$$

Substituting equation (22) into equation (17), the equation for crystal growth velocity, yields:

$$V = V_t \, \frac{T_Y}{|\nabla T|} \qquad (23)$$

At this point, the cooling rate at the solid-liquid interface is readily available:

$$\dot{T}_S = \frac{\partial T}{\partial \hat{r}} \, \frac{\partial \hat{r}}{\partial t} = |\nabla T| \, V \qquad (24)$$

27

The customary notation uses G_L or if it is clear, only G, to denote the temperature gradient pointing into the liquid pool and either V or R to denote the crystal growth velocity. In this report, G and V will be used henceforth and so:

$$\dot{T}_S = G\,V \qquad\qquad (25)$$

2. Construction of the GV Plot

Actual welds will be made at various input power levels and torch velocities, and identical welds will be simulated with the model. The calculated solidification parameters G and V will be correlated with the observed solidification morphology.

The computer model will be run with input parameters identical to the actual welds. Efficiencies close to those estimated by Espinosa [Ref.20] will be assumed. The temperature gradients and growth velocities at the solidifying solid-liquid interface will be calculated.

In order to represent graphically the location where the temperature gradient-crystal growth velocity data pairs (GV pairs) were calculated, a simple transformation will be used. A GV pair calculated at the point P with coordinates (X,Y,Z) will be mapped to the point P' with coordinates (X,Z), as shown in Figure 11. This transformation is possible because the GV pairs will be calculated only on the solidifying front. Therefore, a one to one correspondence between the three dimensional weld pool shape in (X,Y,Z) and the points in the (X,Z) plane exists. This transformation will allow a convenient representation of the entire three dimensional solid-liquid interface on a two dimensional plot. Thus, it will facilitate the correlation between the calculated GV pairs with the macrostructures observed in the weld cross sections.

A GV plot with temperature gradient on the x axis and crystal growth velocity ont the y axis will be constructed. The macrostructure observed at points where the solidification parameters G and V are calculated will be observed and recorded. A symbol representing the macrostructure will be printed on the GV plot at the coordinates G,V.

28
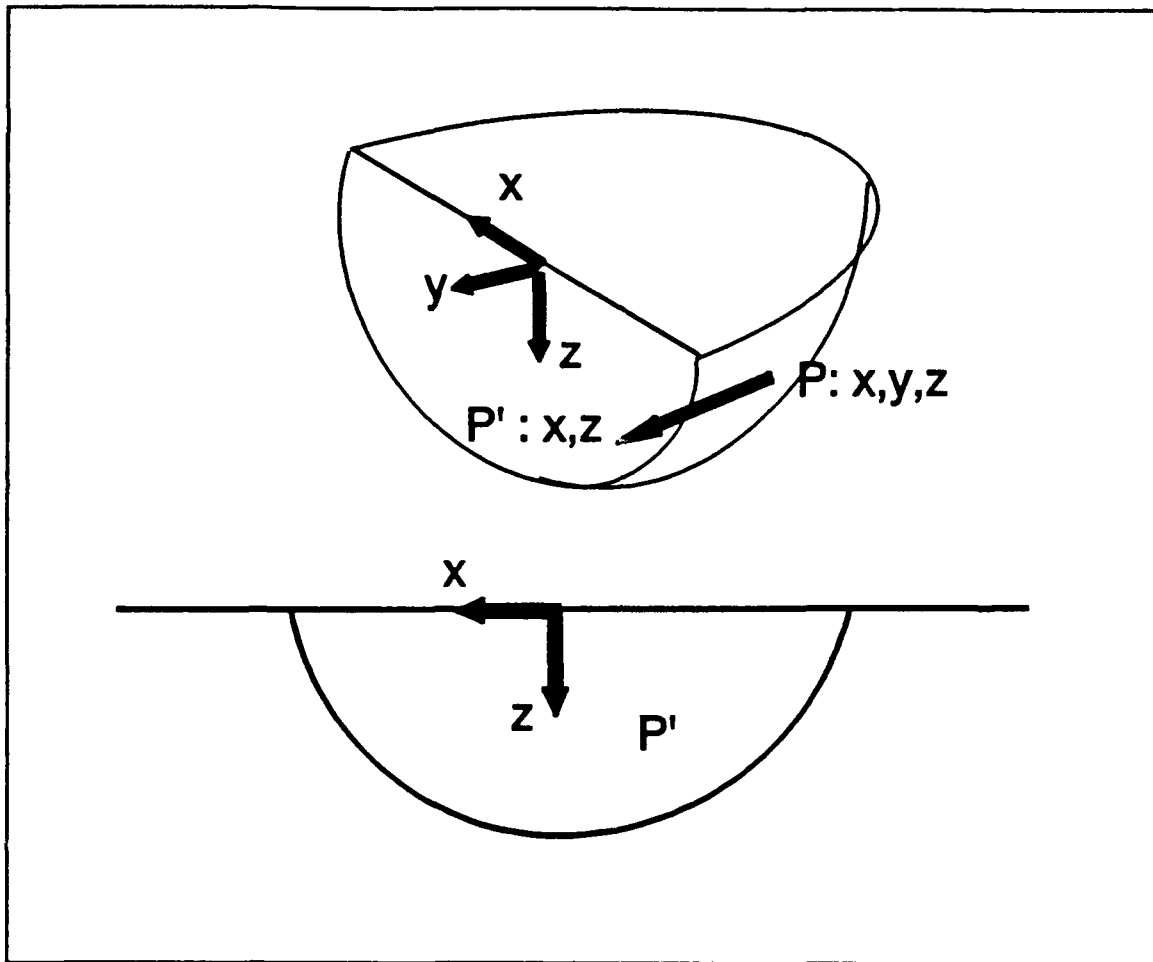
Figure 11 The X,Y,Z to X,Z transformation.

3. Correlation of G and V with Macrostructure

By compiling the data of several welds onto one GV plot, the solidification parameters will be correlated with macrostructure for the alloy being studied.

A strength of this type of correlation is that there is no requirement to estimate the undercooling of the alloy being welded. Quantifying the undercooling would necessitate an extremely accurate compilation of solute segregation and spatial

temperature data. The interdependency of these quantities has been modelled [Ref.18] but is extremely difficult to verify experimentally.

Another strength lies in the fact that although there may be uncertainty in the predicted G and V values, their relative values are approximately correct. Since the numerical model does not account for fluid flow, uncertainty in the results is unavoidable. On the other hand, there is no claim or requirement that the fluid flow be calculated. The only result required by this correlation is the temperature field.

III. EXPERIMENTAL APPARATUS AND PROCEDURE

A. WELDING MACHINE

The welding machine used to generate all the experimental welds was a Miller DC Welding Power Source, Model SR600/SCM1A with Electroslope 3. While the vertical and transverse positioning was performed manually, the longitudinal motion during the weld was controlled by a motorized traverse. Velocity precision was within 0.05 mm/s. For all welds, a tungsten electrode with a 45° tip angle and 4 mm tip spacing was used. Pure argon was the shielding gas, with a flow rate of about 20 cubic feet per hour.

The power settings and uncertainties for each weld run are provided in Table 1. The uncertainty for the linear heat input q was calculated using equation (26):

$$dq = \left(\left(\frac{\partial q}{\partial V} dV \right)^2 + \left(\frac{\partial q}{\partial I} dI \right)^2 + \left(\frac{\partial q}{\partial v_t} dv_t \right)^2 \right)^{1/2} \qquad (26)$$

B. PLATE INSTRUMENTATION

One inch thick HY-80 plates were instrumented with 0.076 mm diameter (0.003 inch, or 3 mils) platinum-platinum rhodium (type S) thermocouples. The smallest practicable thermocouple was selected to minimize the response time. Platinum-platinum rhodium (type S) was chosen because of its high melting temperature. The thermocouples were threaded through ceramic capillaries and inserted in holes which were bored from the underside of the plate, as shown in Figure 12. The capillaries had an outside diameter of 0.1588 cm (1/16 inch). The bore diameter was slightly larger, enabling a snug fit. The capillaries prevented the thermocouple wires from meeting one another and from touching the plate. Bore depths were selected such that 0.5 mm to 6.0 mm clearance

31

TABLE 1 SUMMARY OF WELD SETTINGS WITH UNCERTAINTIES IN PARENTHESES.

run#	V (dV)	I (dI)	v_t (dv_t)	$q = IV/v_t$ (dq)
	volts	amps	mm/sec	Joules/mm
1	14.4 (0.2)	250 (1.0)	3.27 (0.05)	1100 (23.2)
2	14.5 (0.2)	250 (1.0)	2.27 (0.05)	1595 (35.2)
3	13.9 (0.2)	250 (1.0)	1.27 (0.05)	2735 (108.2)
4	13.0 (0.2)	200 (1.0)	2.27 (0.05)	1145 (31.3)
5	12.6 (0.2)	200 (1.0)	3.27 (0.05)	770 (17.4)

remained between the hole and the top surface of the plate. CERMABOND 571, a high temperature, high thermal conductivity epoxy was used to secure the thermocouples in the holes.

C. DATA ACQUISITION SYSTEM

The thermocouples were connected to a high speed voltmeter with automatic ice reference junction compensation in an HP3852A Data Acquisition Control Unit. The HP3852A was controlled by an HP9000 series 300 computer with a 9153C 20Mb hard disk and drive using Basic version 5.13. To reduce the effects of noise caused by the welding machine, the thermocouple channels were guarded and electrical power was supplied via a noise suppression device. A schematic of the apparatus is provided in Figure 13.
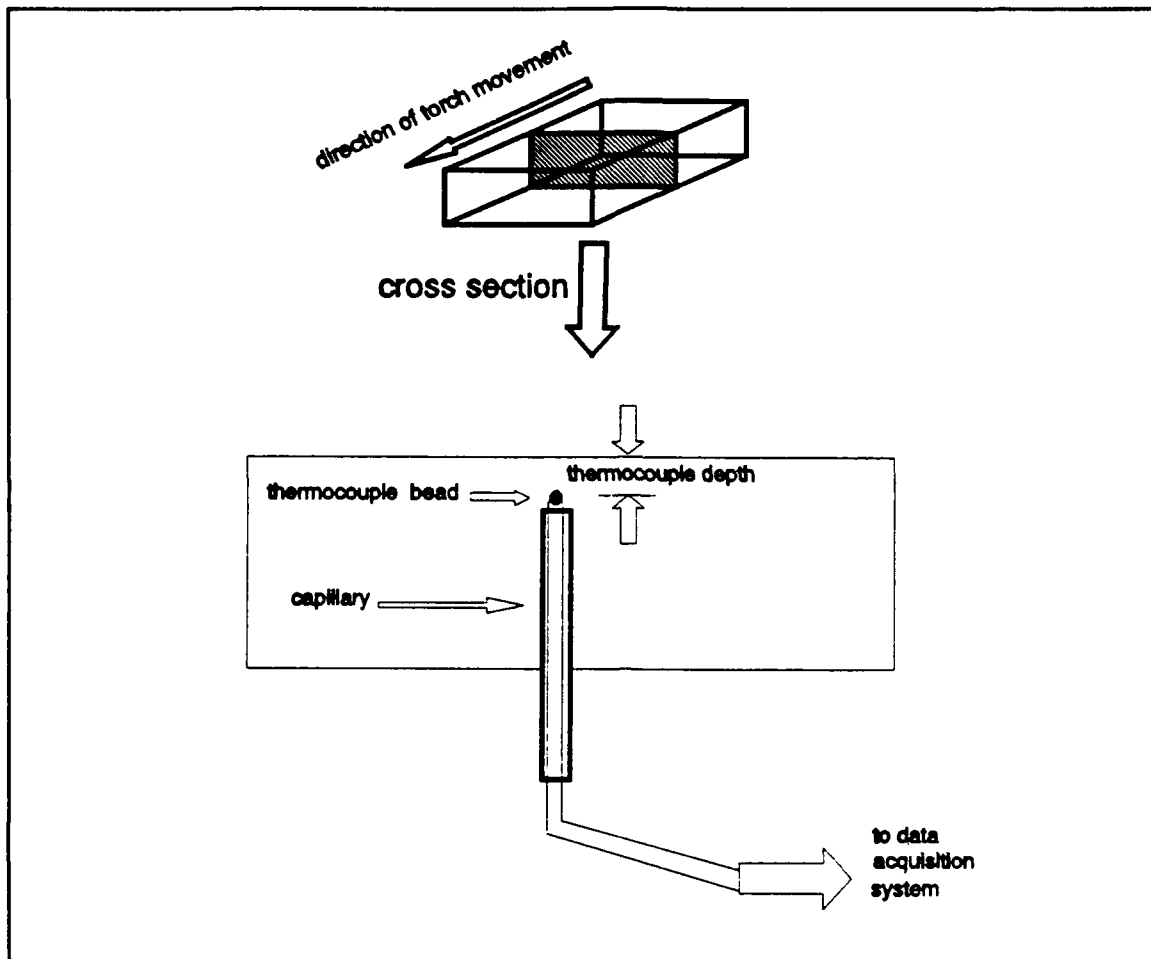
Figure 12 Plate instrumentation. Thermocouples were embedded in the steel plate such that the torch would pass directly over the thermocouple. Thermocouple depths varied from 0.5 to 6.0 mm.

D. METALLURGY

After being cut to suitable sized transverse and longitudinal sections, the samples were prepared by sanding on 240, 320, 400, and 600 grit emery boards. Then the samples were polished using 6 micron diamond paste and 0.05 micron alumina. The samples were etched in a 4 percent Nital solution for 20 seconds before being photographed using Polaroid film and a metallurgical optical microscope and a low power optical stereoscope with oblique illumination.
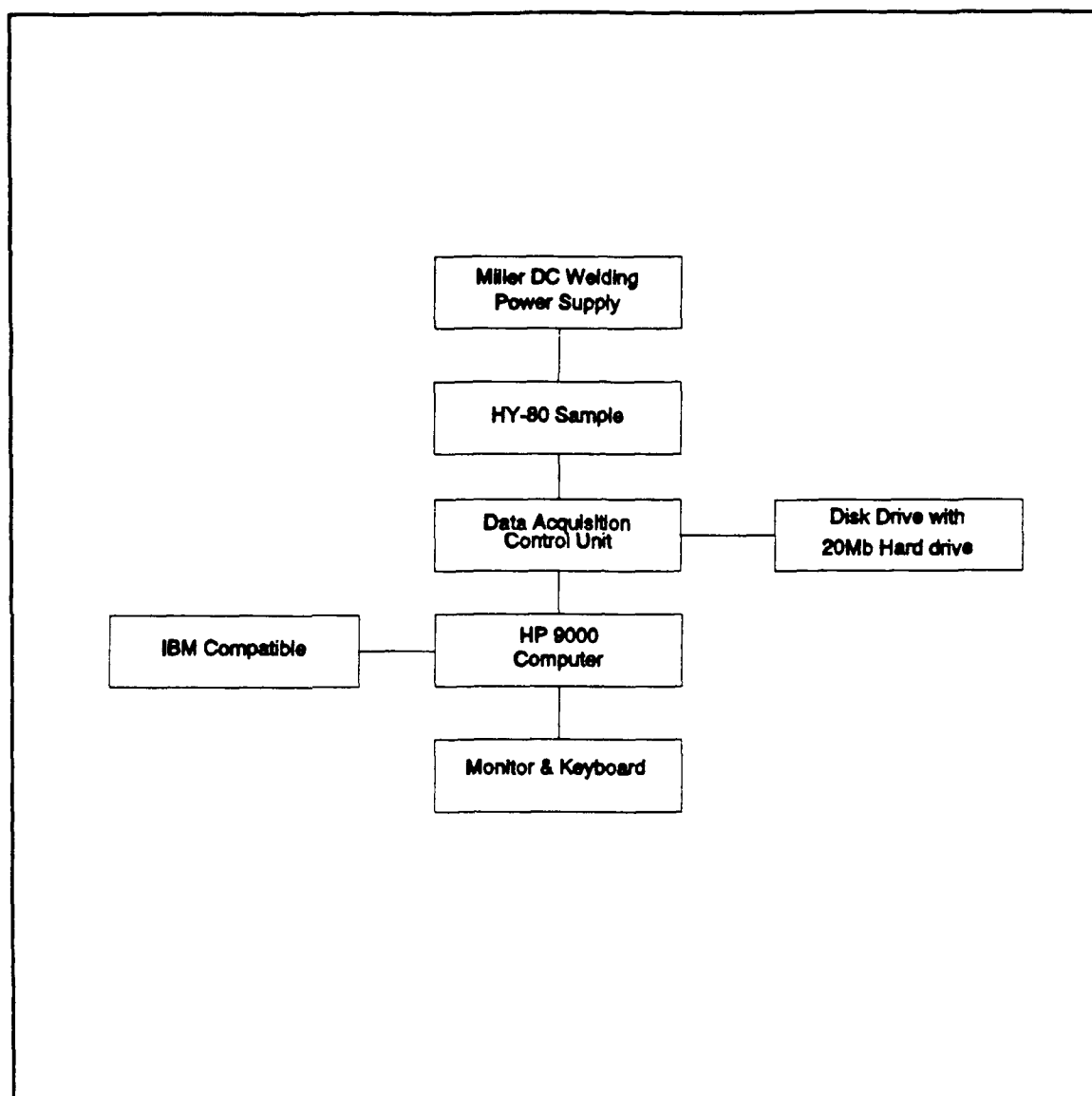
Figure 13 Schematic of the welding apparatus.

IV. RESULTS AND DISCUSSION

A. PRELIMINARY WORK WITH THE NUMERICAL MODEL

Some preliminary work on the model was completed prior to making final calculations of solidification parameters. A melting temperature for HY-80 was selected for all subsequent calculations involving the solid-liquid interface. Time temperature curves predicted by the model were compared with thermal histories measured with embedded thermocouples. The effect of variation in liquid pool thermal conductivity was investigated. For each weld run, the distribution of the heat source in the computations was fine tuned in order that the predicted and measured fusion zone cross sections were geometrically similar. The constant temperature contour which predicted the geometry of the measured heat affected zone was investigated. Finally, the cooling rate as calculated by the product GV was compared to the slope of the predicted time temperature curves. All of this work preceding the calculation of the solidification parameters was done to assess the dependability of the calculated data.

1. Establishing a Melting Temperature

A melting temperature for HY-80 was determined for use in all calculations involving the solid-liquid interface. The melting temperature was used to locate the solid-liquid interface and to calculate the temperature gradient G.

The composition of the material, found by spectral chemical analysis [Ref.20] is provided in Table 2. The effect of each of the alloy elements on the melting temperature was investigated using relevant phase diagrams [Ref.22]. Carbon is the only element which has a significant influence on the melting temperature but the carbon content is slight. A value of 1770K, which is near the middle of the solid + liquid range for the material was selected as the melting temperature for all calculations.

TABLE 2 COMPOSITION OF HY-80 USED FOR ALL WELDMENTS.
THREE SAMPLES WERE ANALYZED. VALUES ARE WEIGHT %.

Element		1	2	3
Aluminum	(Al)	0.03	0.03	0.02
Carbon	(C)	0.14	0.16	0.16
Chromium	(Cr)	1.49	1.46	1.48
Columbium	(Cb)	<0.005	<0.005	<0.005
Copper	(Cu)	0.10	0.04	0.03
Manganese	(Mn)	0.23	0.30	0.30
Molybdenum	(Mo)	0.37	0.36	0.38
Nickel	(Ni)	2.79	2.52	2.52
Nitrogen	(N)	0.015	0.009	0.009
Phosphorus	(P)	0.01	0.007	0.007
Silicon	(Si)	0.25	0.25	0.25
Sulphur	(S)	<0.005	0.018	0.017
Tin	(Sn)	0.009	<0.005	<0.005
Titanium	(Ti)	<0.005	<0.005	<0.005
Vanadium	(V)	<0.005	<0.005	<0.005

2.   Comparison of Calculated and Measured Time Temperature Curves

Time temperature curves for welds were measured using embedded thermocouples. The thermocouples were positioned both inside and outside the anticipated weld pool. The success of measuring the temperature histories in the weld pool was limited. For runs with thermocouples allegedly positioned in the weld pool, two results were common:

1. Data collection ceased when the torch passed over the thermocouple. Temperature curves during heating were measured but the thermocouple was rendered inoperab prior to cooling. Whether due to high temperatures, exposure to the arc, or interaction with the liquid metal, the thermocouples were not functional after the torch passed.

2. The maximum temperature never exceeded the melting temperature of the alloy. By trying to position the thermocouples close to the anticipated fusion line, chances of surviving were improved but sometimes the weld pool was missed.

The temperature histories which were measured were compared to the results predicted by the model. The heating portion of a curve measured by a thermocouple which did not survive the weld run is compared with a predicted temperature history of a node point in the weld pool. The result is Figure 14. The predicted and measured results are in very good agreement.

Figure 15 shows the measured time temperature curve for a point in the weld metal outside the fusion zone compared with results predicted by the model for a corresponding node point. Again, the agreement is good.

3. The Effect of Variations in Weld Pool Thermal Conductivity

In the numerical model, the thermal conductivity corresponding to nodes in the fine mesh zone is a function of temperature. The function is based on physical data [Ref.23] except when temperatures exceed the melting temperature. The thermal conductivity in the molten metal is inflated to account for convection heat transfer.

For several simulations, all parameters in the model were held constant except for the fusion zone thermal conductivity, which was varied over a wide range. The calculated fusion zone sizes were compared with the fusion zone size measured on an actual weld. The results are presented in Figure 16.

As seen in Figure 16, there was a negligible change in the size of fusion zone as a result of variations in weld pool thermal conductivity. At certain conductivities, however, the shape of the fusion zone began to change. When the thermal conductivity

37
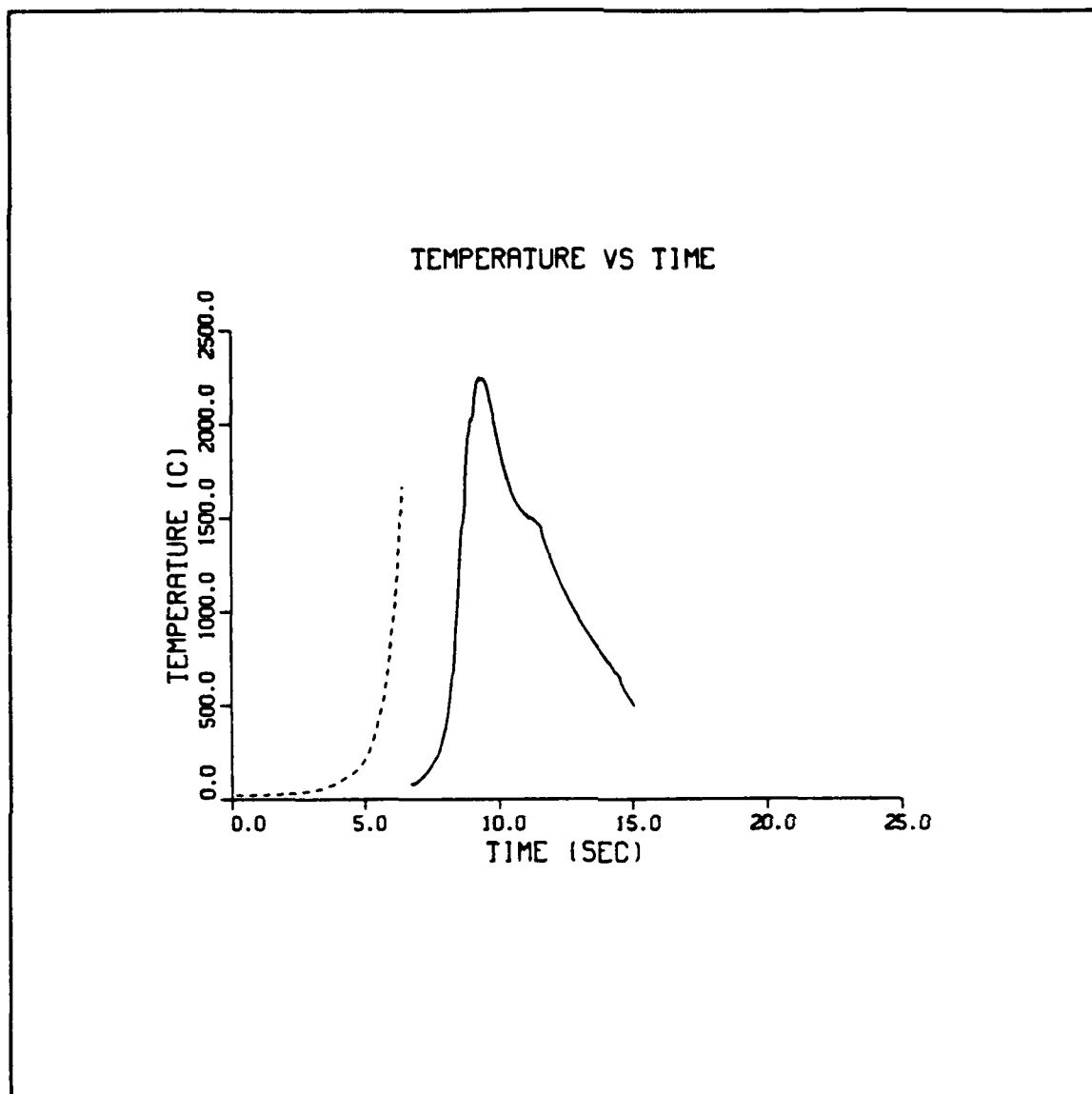
Figure 14 Time temperature curve for a point in the weld pool. The dashed line represents measured values. The solid line represents computed values. The curves are time shifted for ease of viewing.

was increased above 125 W/mK, a waviness in the fusion line developed, which appears to be due to numerical instabilities. The waviness was very pronounced when the conductivity was set to 250 W/mK. When thermal conductivity was set to 500 W/mK, the computer run halted on an error.

For subsequent runs, a moderate value of 100 W/mK for thermal conductivity in the weld pool was used.
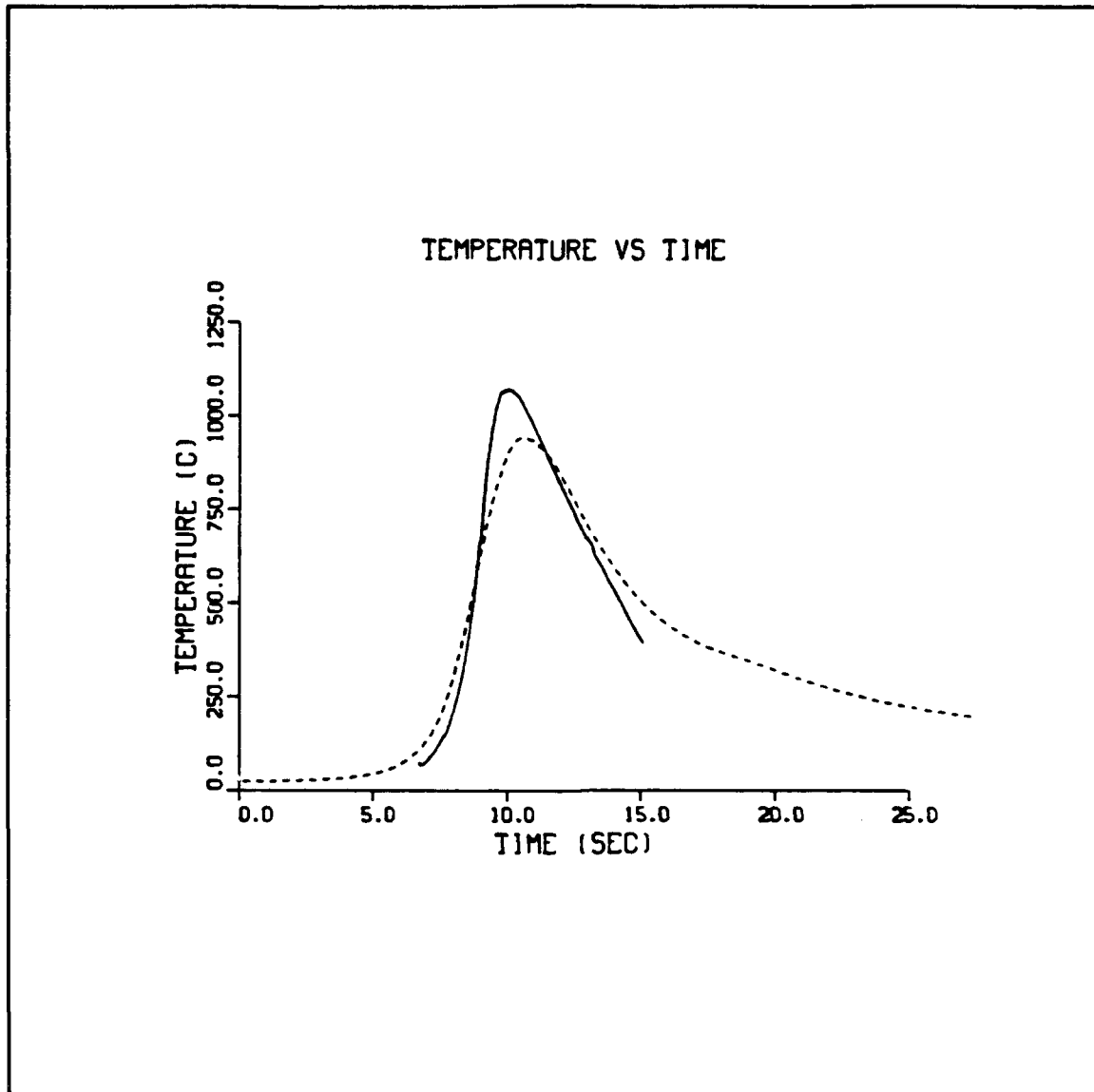
Figure 15 Time temperature curve for a point outside the weld pool. The measured curve (dashed line) was taken by a thermocouple positioned outside the weld pool. The solid line represents computed values for a point nearby.

4. Fine Tuning the Heat Input Configuration

Prior to using the temperature field data predicted by the model to calculate solidification parameters, the variables which effect the heat distribution were manipulated in order to achieve a close match of the predicted and calculated fusion cross

39
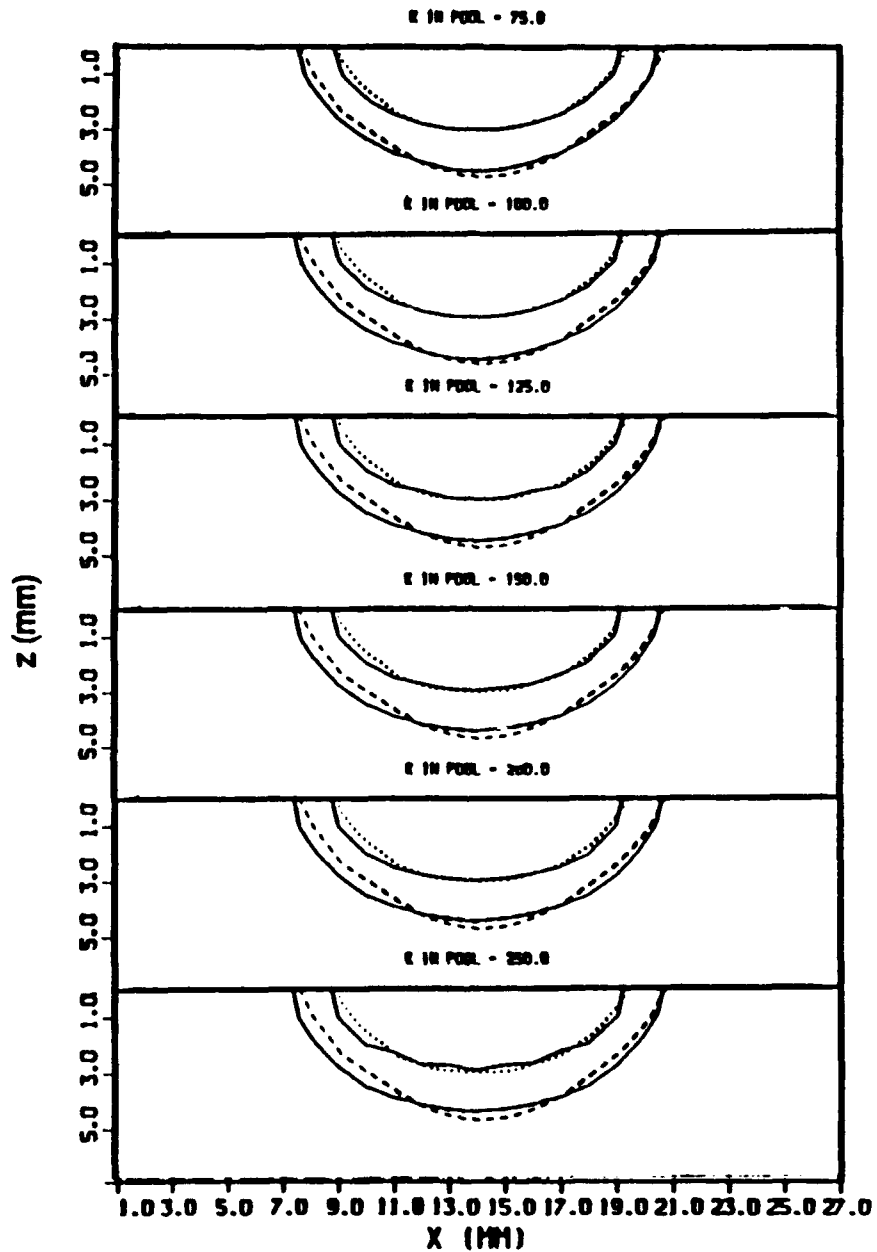
Figure 16 Effect of variation in weld pool effective thermal conductivity. The solid lines are computed. The dotted line is the measured fusion zone. The dashed line is the measured heat affected zone.

40

section geometries. In the source code, the variables which control the Gaussian volumetric heat distribution, A1, B1, and C1 for the X, Y, and Z directions, respectively, are user specified (See Chapter II, Section A, Subsection 2). The effect of increasing any of these is to introduce a greater fraction of the torch power to the respective direction, and to cause the heat intensity to fall off more slowly along that direction.

Increasing A1 caused the weld pool to be wider and shallower. In the original configuration, the predicted weld pool cross section was narrower and deeper than the observed cross section, as seen in Figure 17a. A1 was increased until the width of the pool was approximately correct, as shown in Figure 17b and Figure 17c. The numerical values of A1 are listed in Table 3. A 5% downward adjustment in the weld efficiency used by the model brought the predicted and observed fusion zone geometries into very close agreement, as illustrated in Figure 17d. Figure 18 shows that for each weldment, a good agreement between the predicted and measured fusion and heat affected zone was achieved.

TABLE 3 NUMERICAL VALUES OF A1 AND THE RESPECTIVE PART OF FIGURE 17.

A1	4.0	7.0	8.0	8.0
figure 17	(a)	(b)	(c)	(d)

5. Determination of the Constant Temperature Contour which Predicts the Fusion Zone Geometry

For each of the cross sections given in Figure 18, the constant temperature contour chosen to represent the heat affected zone was changed. If the material were heated and allowed to cool very slowly, the temperature contour which predicted the heat
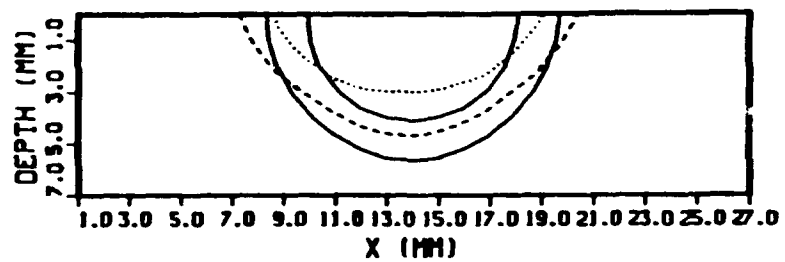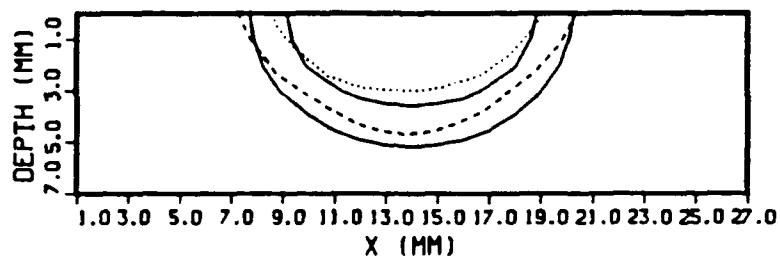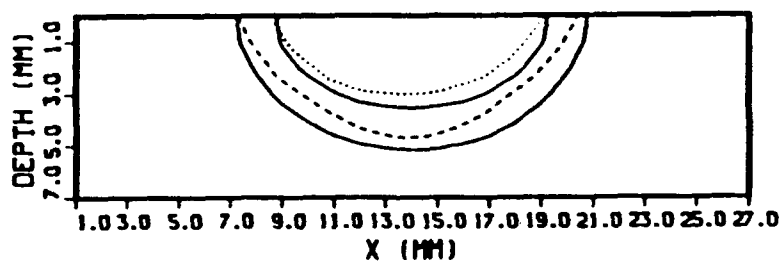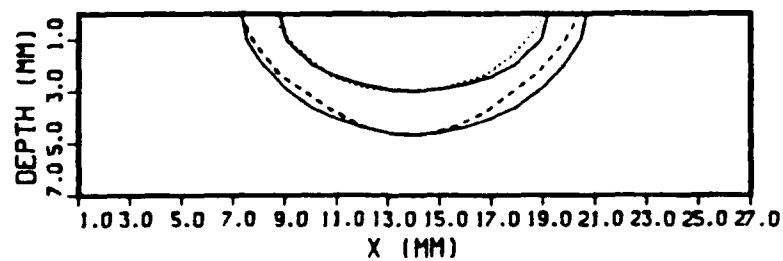
Figure 17 Effect of variation in modelled heat input configuration. The heat input configuration was fine tuned until the predicted and measured fusion zone geometries were in agreement.
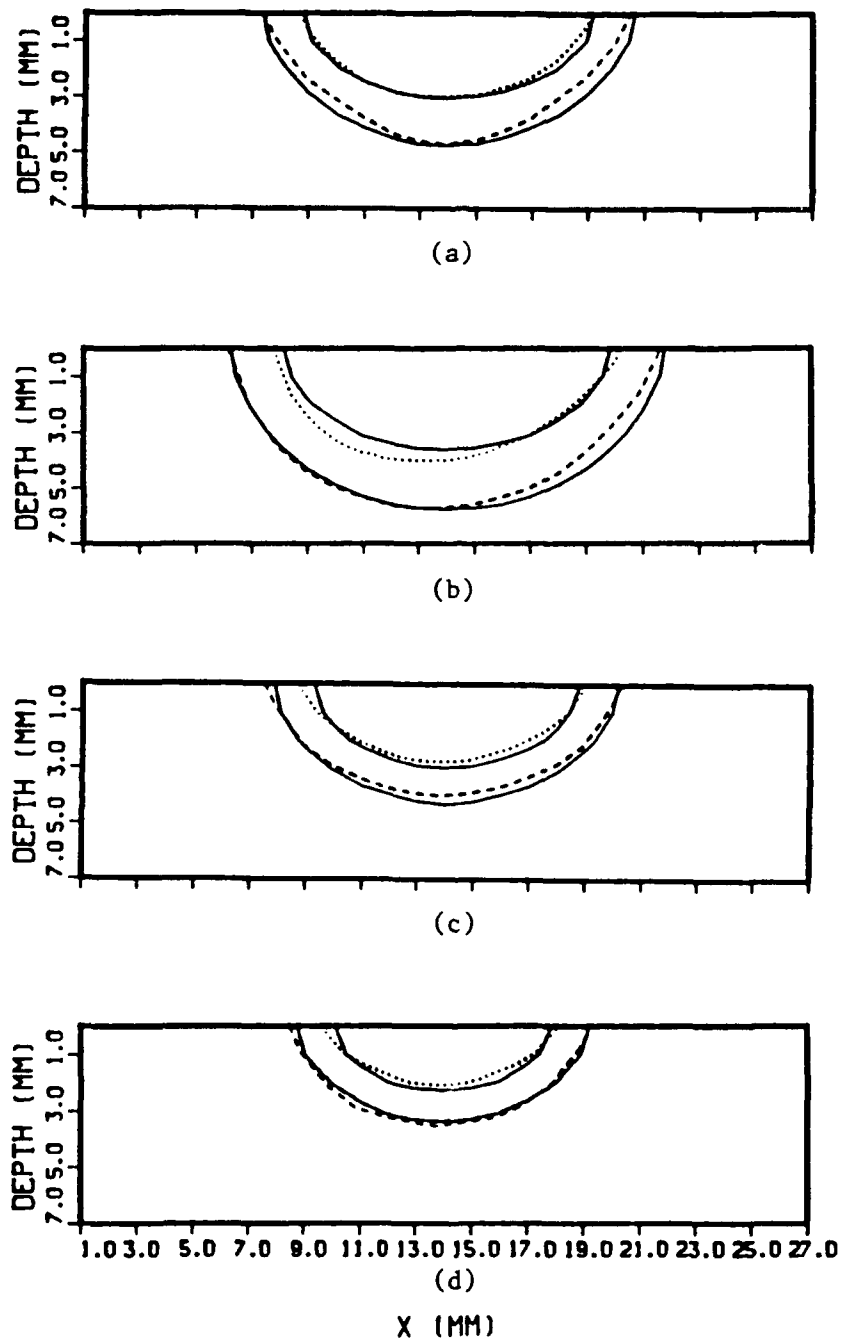
Figure 18 Fusion zones of all weldments. Predicted (solid lines) and measured (dashed lines) fusion zones and heat affected zones for (a) Weldment one; (b) Weldment two; (c) Weldment four; (d) Weldment five.

43

affected zone would be very near the austenite transformation temperature. However, since there are short cooling times experienced by the material surrounding the weld pool, the temperature contour which predicts the heat affected zone is substantially higher than the austenite transformation temperature. The shorter time at high temperature requires a higher temperature for the transformation to take place. The variation in the predicted effective heat affected zone temperature with input power is shown in Figure 19. As expected higher input powers corresponded to lower predicted effective heat affected zone temperatures.
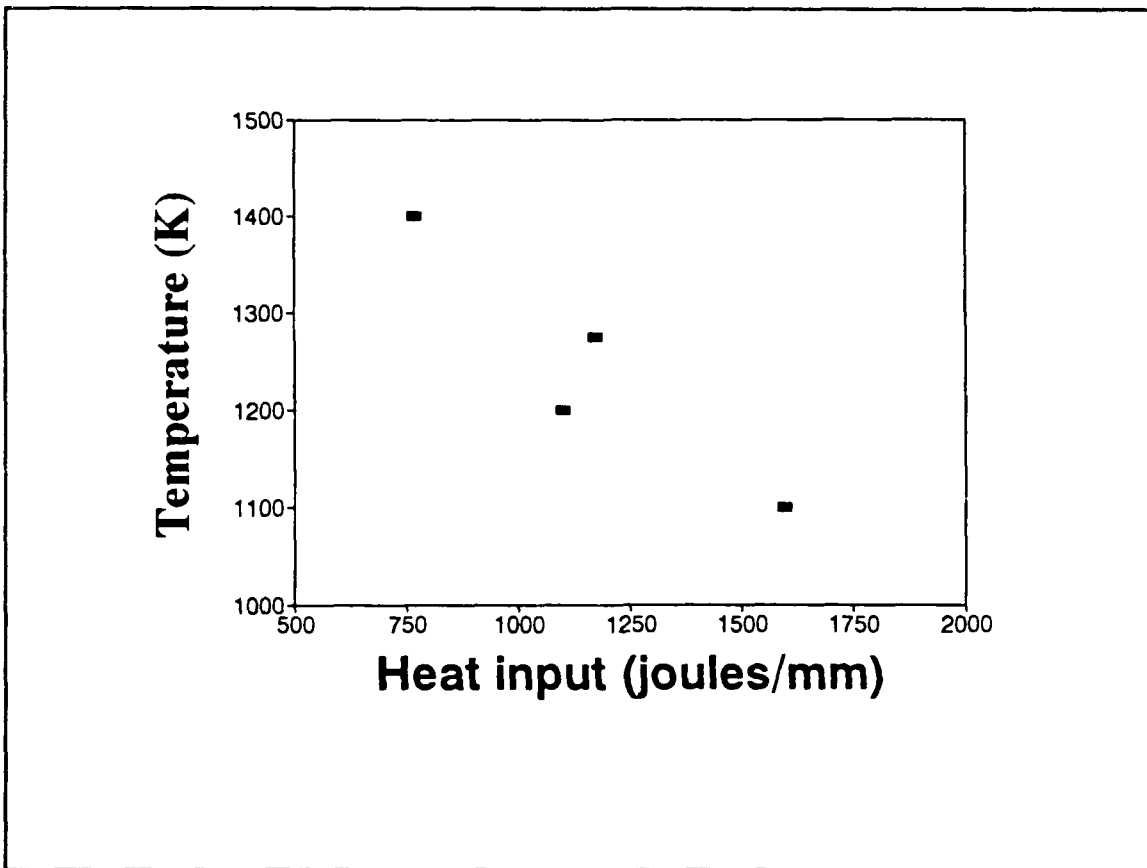
Figure 19 Variation of the effective heat affected zone temperature with heat input.

6. Interpretation of the Product GV

Predicted time temperature curves for three points in the fusion zone are given in Figure 20. The product GV, the cooling rate, was also calculated at each of the points. The dashed line in Figure 20 was drawn with slope GV at the point in the cooling curve where the predicted cooling rate equalled GV. The cooling rate GV corresponds to a time in the predicted time temperature curve very near the arrest point. Figure 20a corresponds to a point near the fusion line. Figure 20c corresponds to a point near the weld centerline. Figure 20b corresponds to a point between those of (a) and (c).
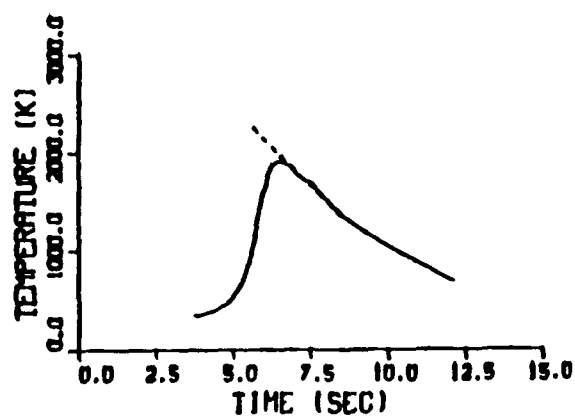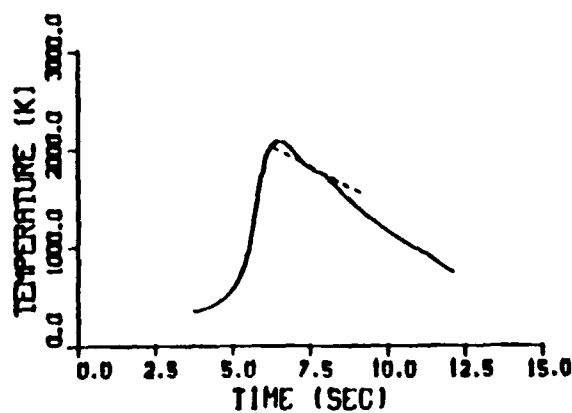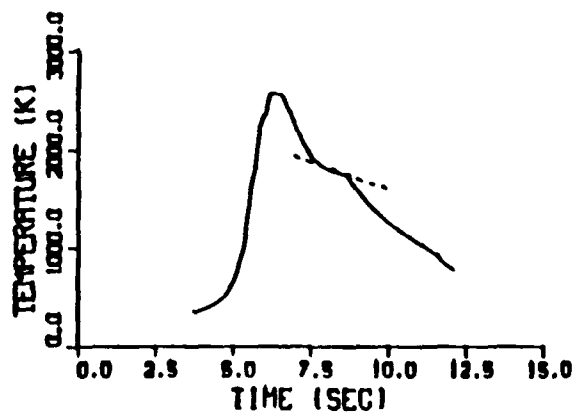
Figure 20 Interpretation of the product GV. Time temperature curves with a line of slope of GV drawn tangent.

B.   CALCULATED SOLIDIFICATION PARAMETERS

Once the calculated and observed fusion zone geometries were in agreement, as shown in Figure 18, the predicted temperature field data was used to calculate the solidification parameters G and V.

The solid-liquid interface was located by looping through all X,Y values in the fine zone. For each X,Y value, the vertical fusion penetration depth was found by interpolating between node points whose temperatures indicated the presence of the solid-liquid interface. Then, the components of temperature gradient were calculated using equations (18)-(20), which are of the form:

$$T(X+\delta X, Y+\delta Y, Z_m+\delta Z) = T(X, Y, Z_m) + T_X \, \delta X + T_Y \, \delta Y + T_Z \, \delta Z \tag{27}$$

Z_m is the interpolated vertical position of the solid-liquid interface on a line of constant X,Y.

After the three components of temperature gradient were calculated, the magnitude of the temperature gradient G and the crystal growth velocity V were calculated:

$$G = (T_X^2 + T_Y^2 + T_Z^2)^{1/2} \tag{28}$$

$$V = \frac{T_Y}{G} \, V_t \tag{29}$$

A GV pair calculated at (X,Y,Z_m) was considered to be the solidification parameters for the point in the fusion zone transverse cross section (X,Z_m). An index was assigned to each of the GV pairs and plotted directly on the calculated fusion zone cross section as in Figure 21. A comprehensive table of all data at each of the points was printed for each weld run. The table includes the calculated solidification parameters, and

47

fusion zone penetration depth at each discrete point on the solid-liquid interface. The tables may be found in Appendix I.
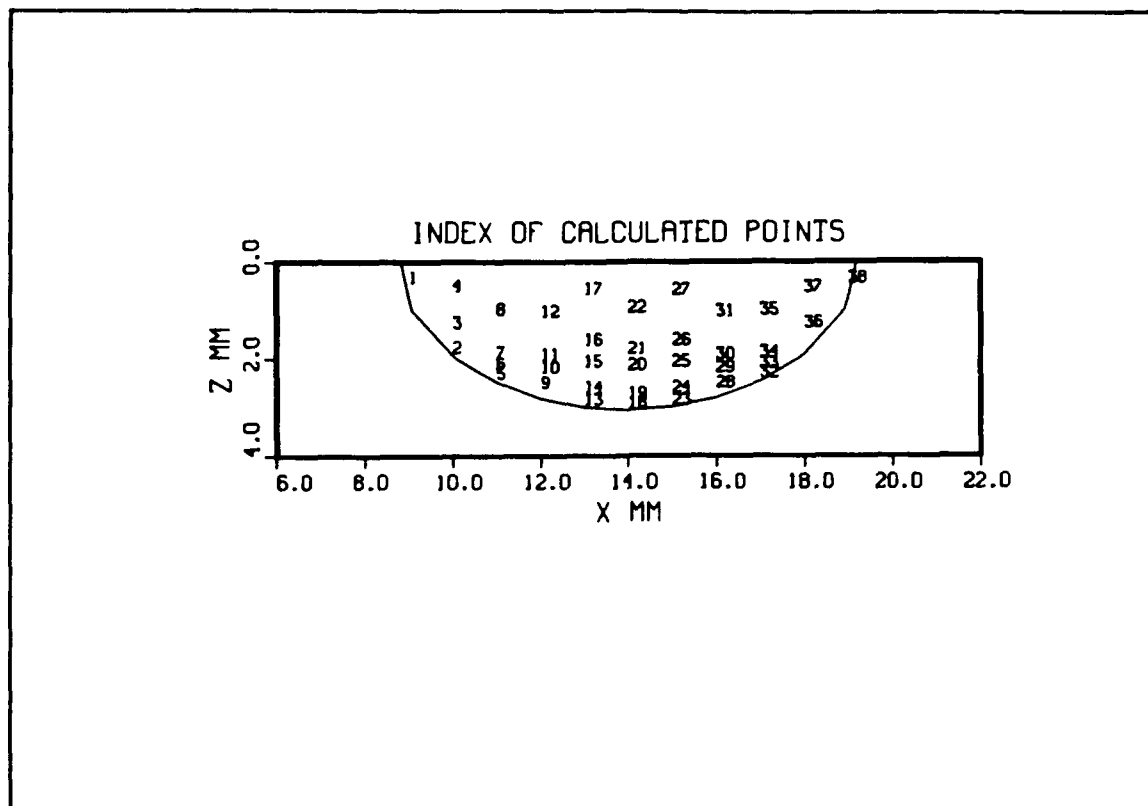
Figure 21 An example of the presentation of the indices of calculated points. At each index, the solidification parameters G and V were calculated.

GV plots were constructed: a log-log plot with G on the horizontal axis and V on the vertical axis. The GV plot which David and Vitek presented [Ref.1] is given above in Figure 10. The bold arrow indicates the results one would expect when taking data at the fusion line and moving toward the weld centerline. The quantified GV plots prepared in this study are provided in Figure 22 through Figure 25. The results predicted by the model clearly agree with the expected results. Results for weldment three are not presented. Weldment three was made at a very high heat input. Time increment independence was not achieved in the computer simulation.

48

Furthermore, the range of values predicted here are supported by those given in the literature. Gradients of 72 K/mm to 275 K/mm for arc welds on steels have been reported [Ref.1].
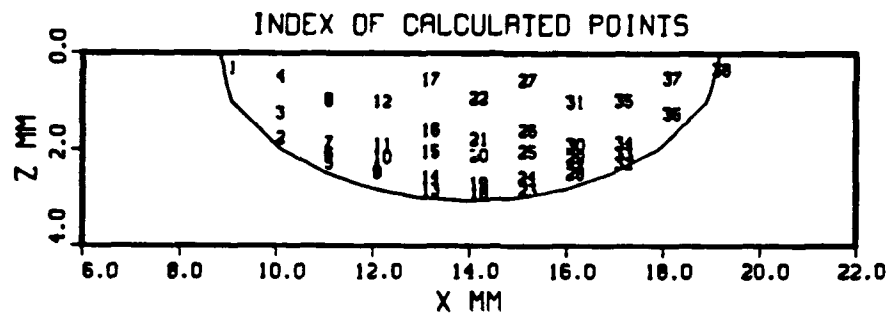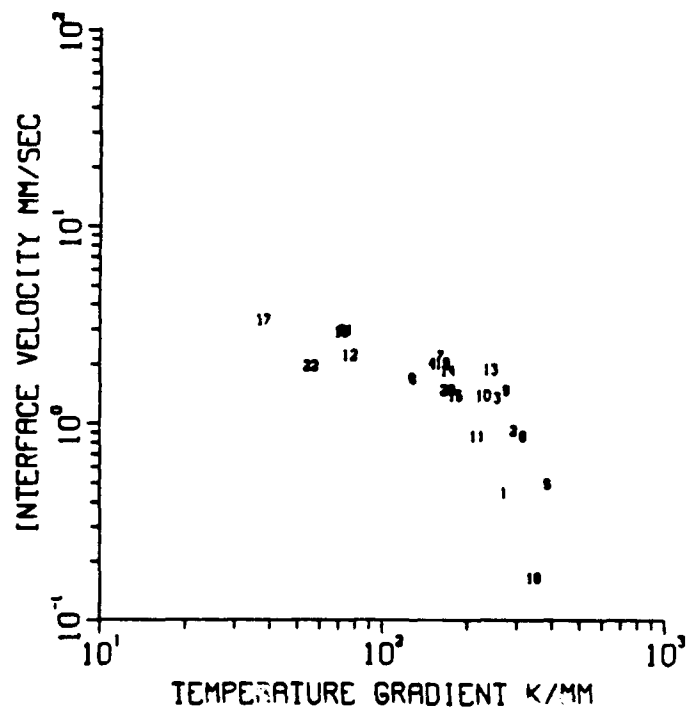
Figure 22 GV plot for weldment one.
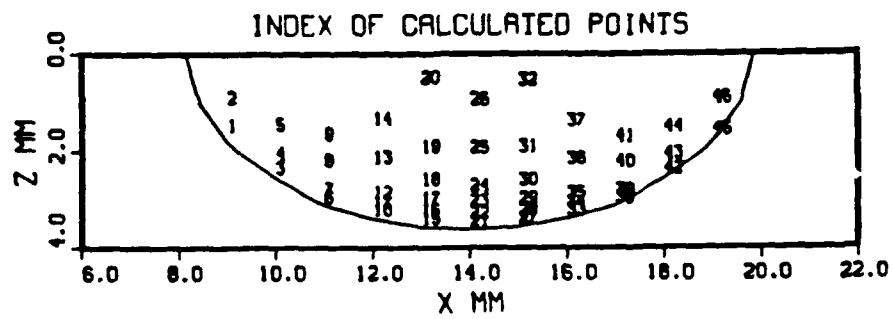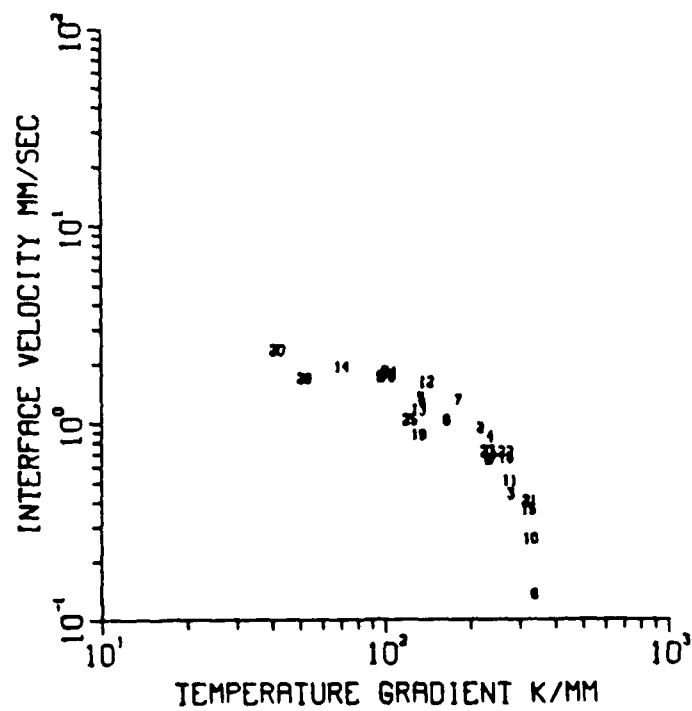
Figure 23 GV plot for weldment two.
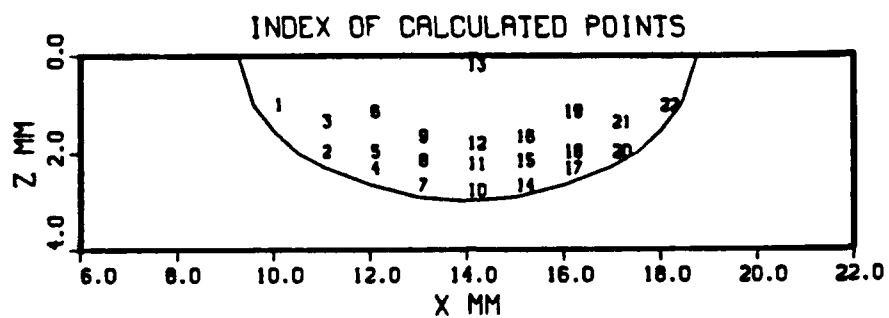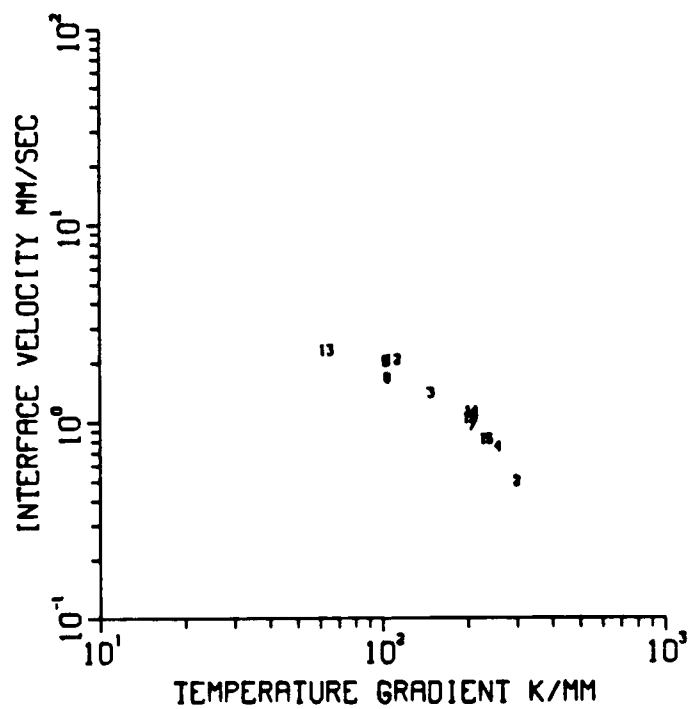
Figure 24 GV plot for weldment four.
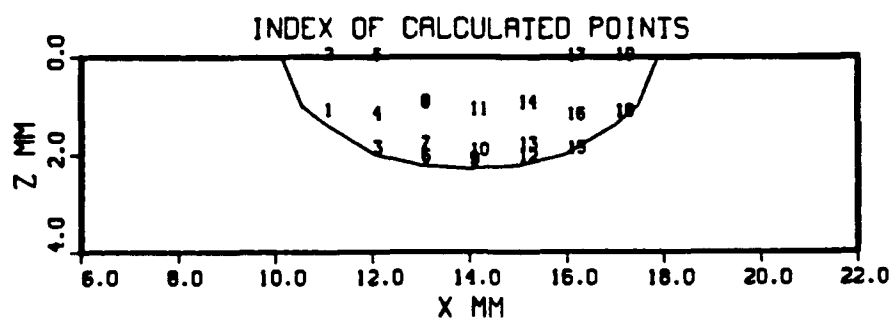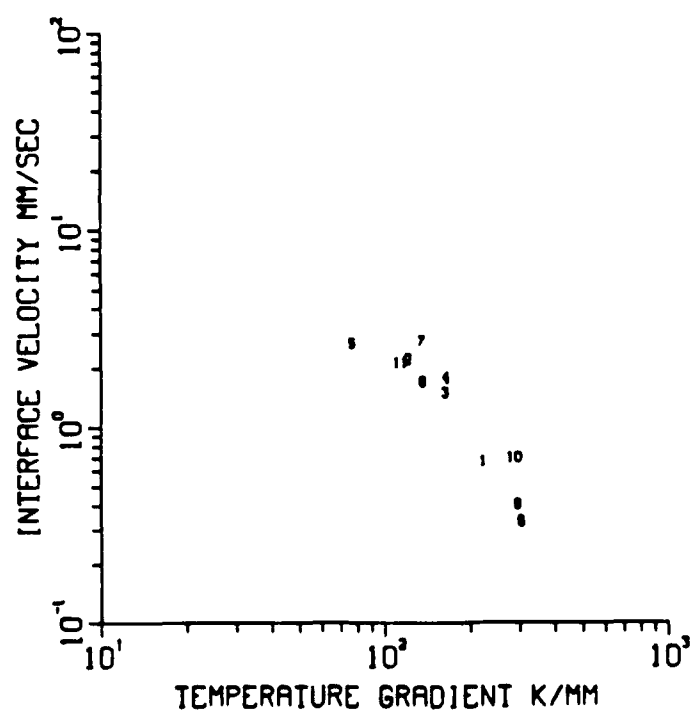
Figure 25 GV plot for weldment five.

C. METALLURGICAL RESULTS

1. Macrostructure

The macrostructures of the samples were evident at low magnifications (20X or less) on a stereoscope. Photographs of the top surfaces and transverse surfaces of samples from weldments one, two, four, and five are provided in Figure 26 through Figure 29. The top surfaces of all four weldments show a thin region of planar growth near the fusion line. Inside the planar growth region, equiaxed crystals and columnar crystals were found but the size and orientations varied significantly between weldments.

The top surface of weldment one has long columns growing toward the weld centerline and bending toward in the direction of torch movement. At the centerline, there are very long columns parallel to the torch movement. Figure 30, taken near the top surface centerline of weldment one, shows where the two distinct sets of columns meet. The long columns along the left border are the columns growing parallel to the torch movement. Figure 31, taken near the top surface fusion line, shows that the columns began to grow very near the fusion line, without an appreciable region of equiaxed crystals.

The transverse view of weldment one also revealed mostly columnar crystals, but with some equiaxed crystals near the fusion line. The dominance of columnar growth in weldment two is explained by the relatively high power and high velocity. While the temperature gradient and growth velocity is influenced by both input power and torch velocity, the most significant effect of high power is lower temperature gradients and the high torch velocity forces rapid growth rate. This combination leads to a low G/V ratio, favoring columnar growth.

Weldment two, viewed from the top, has very fine columnar crystals growing toward the center and bending slightly in the direction of torch movement, as shown in Figure 27. The centerline serves as a meeting place for the columns but is not characterized by the long columnar crystals found on weldment two. Figure 32 shows
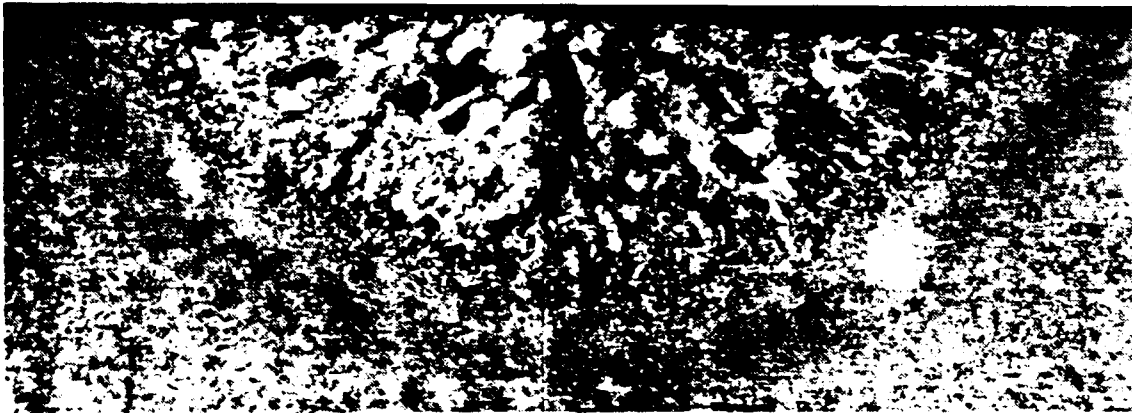
Figure 26 Photomicrographs of Weldment one. The top view at 8X and the transverse section at 14.6X.
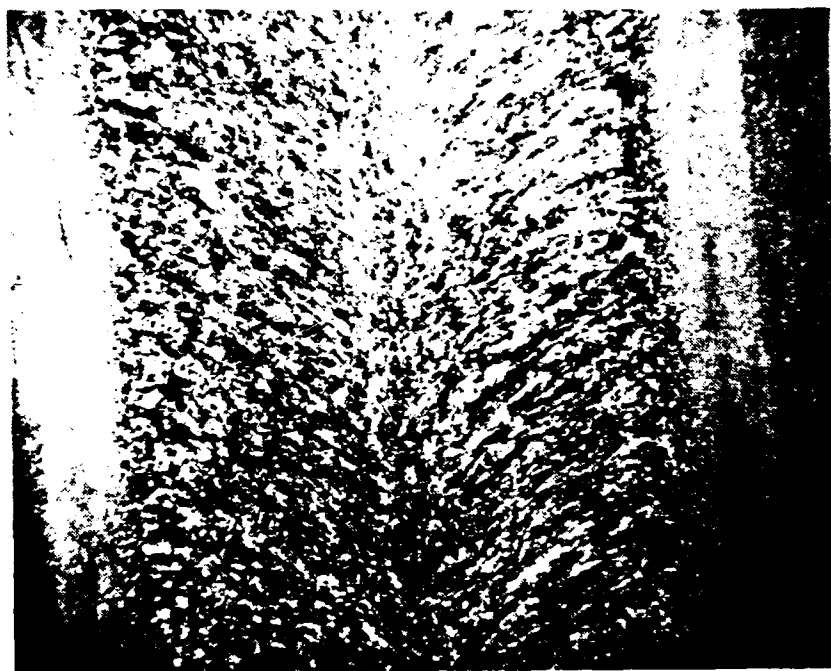
Figure 27 Photomicrographs of weldment two. The top view at 8X and the transverse section at 11.6X.
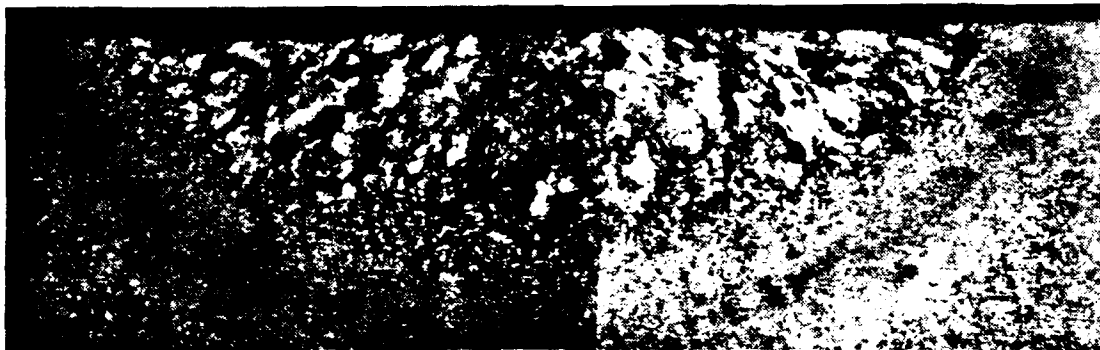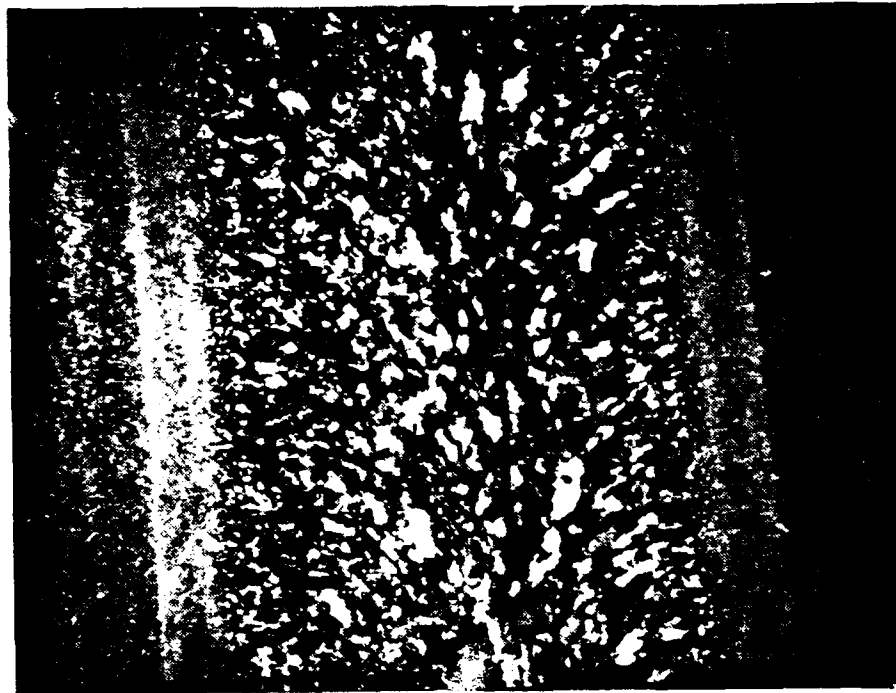
Figure 28 Photomicrographs of Weldment four. The top view at 8X and the transverse cross section at 14.5X.
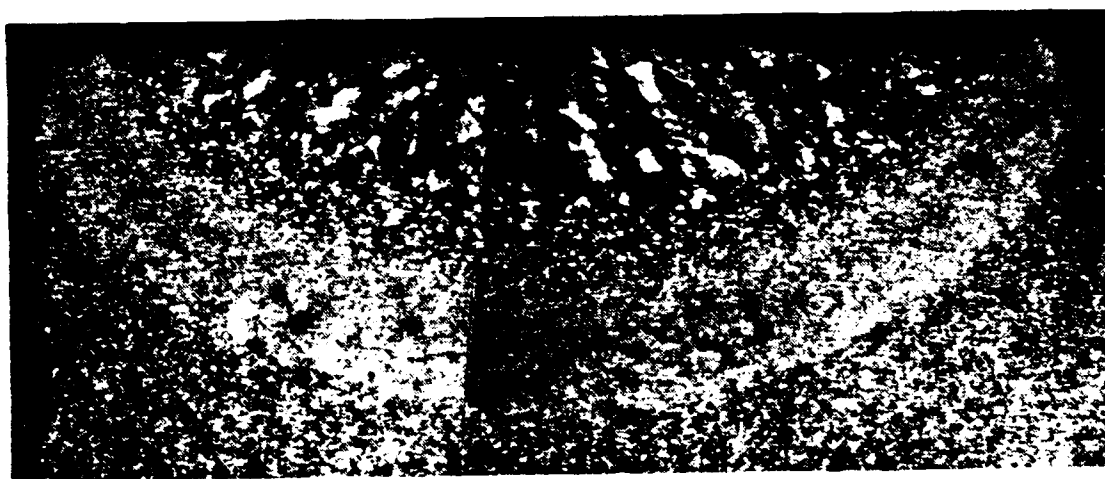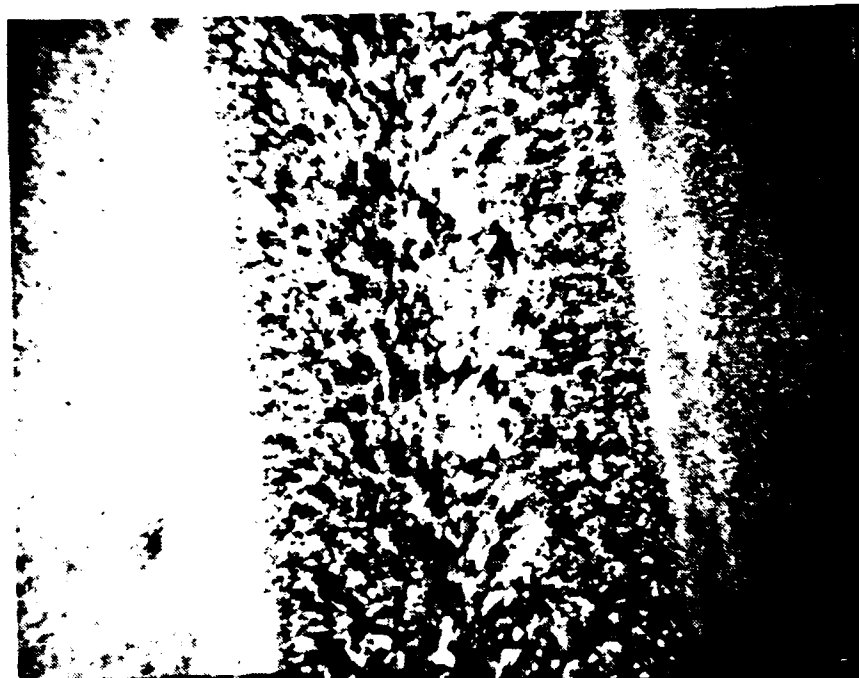
Figure 29 Photomicrographs of Weldment five. The top view at 8X and the transverse section at 15.5X.

58

Figure 30 Photomicrograph. Weldment 1 top surface near centerline. 50X.

the columnar crystals growing toward the top surface centerline. The centerline is distinct only because it appears less columnar. Figure 33 shows that there is a region of equiaxed crystals near the fusion line of weldment two.

This region of equiaxed crystals appears along the fusion line of the transverse section of weldment two as well, as shown in Figure 27. Near the centerline is a macrostructure which is either fine equiaxed crystals or fine columns viewed from the end. The power settings for weldment two were about the same as for weldment one, but the torch velocity was considerably slower. Therefor .alitatively, the gradients of weldment one should be nearly those of weldment two : the growth velocity will be less. Thus, a lower G/V ratio, which explains the reduction in the dominance of columnar crystals.

59
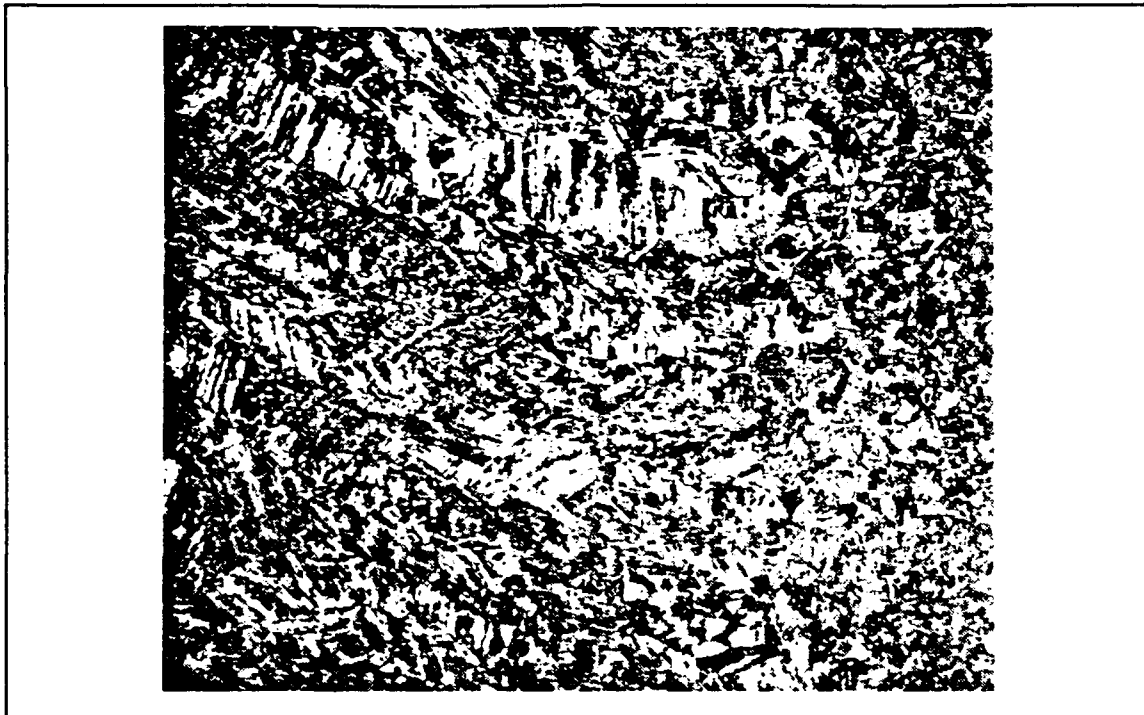
Figure 31 Photomicrograph. Weldment 1 top surface fusion line at 50X.

Both the power and torch velocity were relatively low in the case of weldment four. The top surface is mostly equiaxed crystals. There are some hints of columnar crystals in that some of the crystals are elongated, as in Figure 34 and Figure 35, taken near the top surface centerline and fusion line, respectively.

Columnar crystals are more evident in the view of the transverse section of weldment four than the top view. However. there is still a mix of columnar and equiaxed crystals.

The top surface of weldment five, Figure 29 (upper photomicrograph) is very similar to that of weldment four except that the tendency for the crystals to be columnar is more pronounced. The same is true of the transverse sections. Weldment four was a mix of equiaxed and columnar crystals while weldment five is more columnar. The power setting for run one was similar to that of weldment four but the torch velocity was higher, explaining the increased presence of columnar crystals.
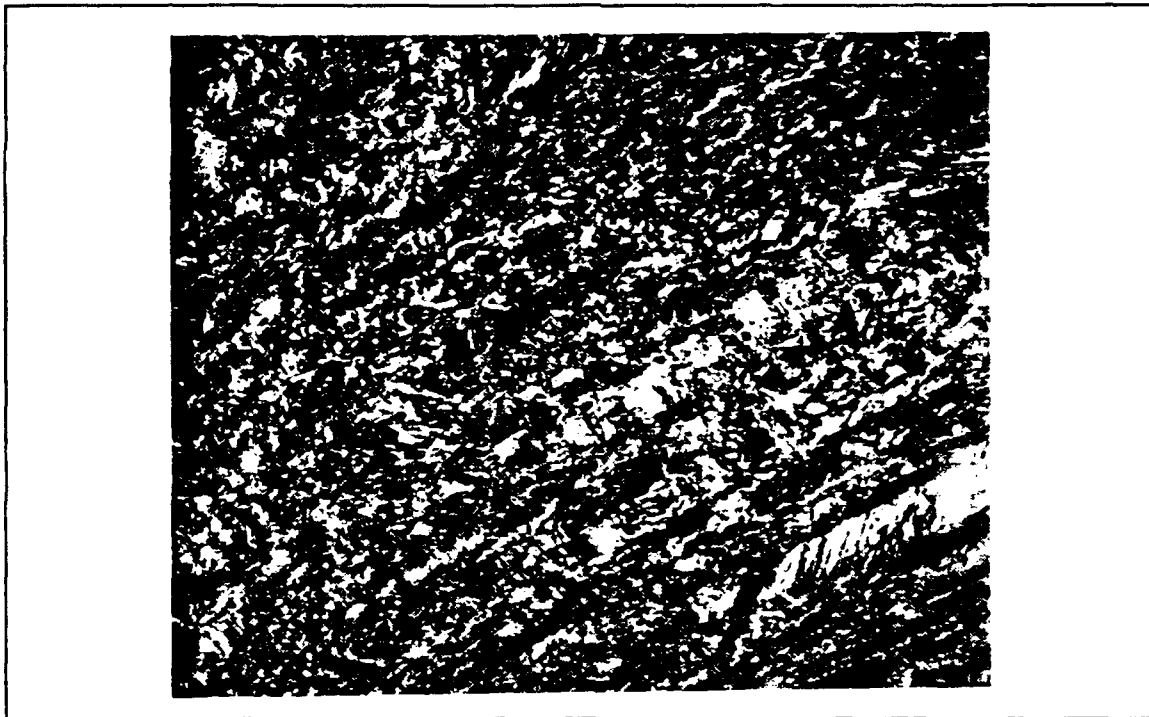
Figure 32 Photomicrograph. Weldment 2 top surface near centerline. 50X.

2. Substructure

Viewing the substructure required higher magnifications than the macrostructure and required reflected light microscopy. Although the substructure was often discernible at 50X magnification, important features were better viewed at 200X to 500X.

A region of planar growth was present at the fusion line of each weld. Just inside this region, the solidification modes under constitutional undercooling were active. Figure 36, taken in the middle region of the transverse section of weldment one, illustrates the presence of cellular growth. Figure 37 clearly shows the presence of columnar/dendritic growth.
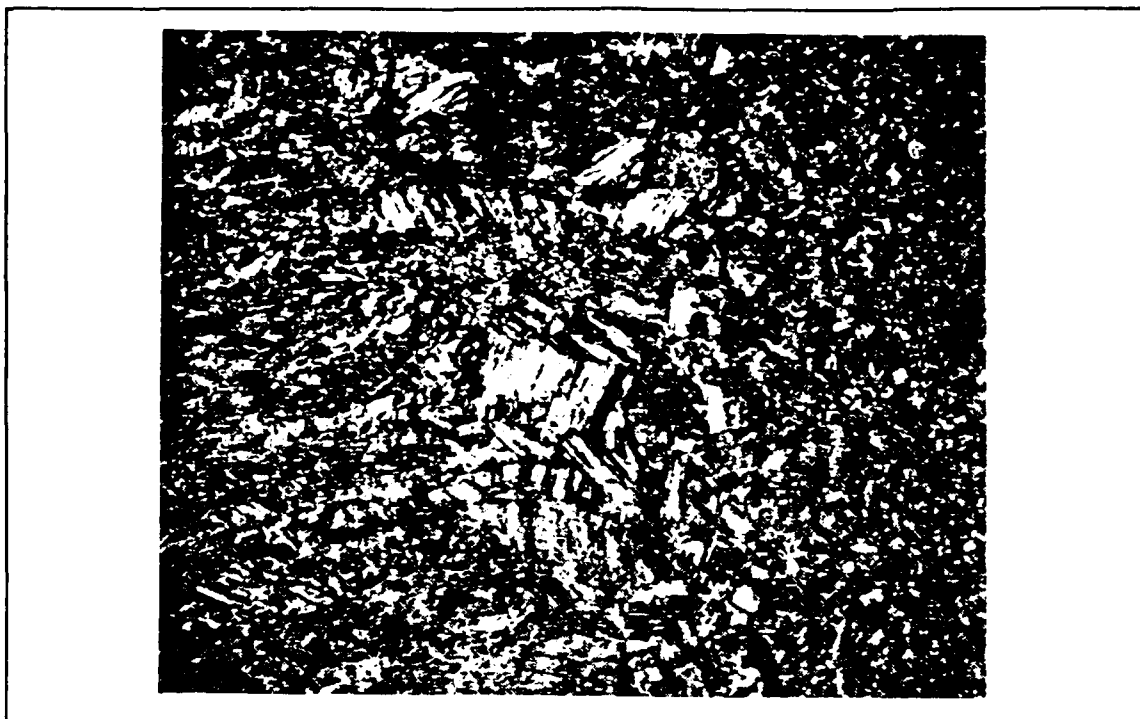
Figure 33 Photomicrograph. Weldment 2 top surface near fusion line. 50X.

D. CORRELATION OF SOLIDIFICATION PARAMETERS WITH MORPHOLOGY

1. Macrostructure

The calculated solidification parameters G and V were correlated with the macrostructure of the observed welds. To present the macrostructure in terms of the solidification parameters, the macrostructure was observed and recorded at each of the points where the solidification parameters were calculated. The low power stereoscope at magnifications of 20X to 50X was used. When feasible, the macrostructure on the top surfaces of the samples were observed for clarification or confirmation of transverse cross section macrostructures.

Upon completion, a data base was compiled consisting of three columns: the temperature gradient, the growth velocity, and a symbol to denote the macrostructure: 'P'=planar; 'E'=equiaxed crystals; and 'C'=columnar crystals. A GV Plot was

62

Figure 34 Photomicrograph. Weldment 4 top surface near centerline. 50X.

cons' ucted and is presented in Figure 38. The symbols representing observed macrostructures were printed at their respective GV coordinates.

There are regions of the plot which clearly indicate solidification conditions which lead to a specific macrostructure. At points falling in the lower right portion of Figure 38, where the G/V ratio is high, mostly planar macrostructure was observed. These points were exclusively at the perimeter of the transverse weld section just inside the usion line. In the upper left portion, where G/V is low, columnar macrostructures were dominant. Mostly equiaxed crystals were observed between the extreme values of G/V These results are in agreement with the results proposed in the literature shown in Figure 10.

As expected, there is overlap of the regions rather than distinct borders. The transition from a planar to equiaxed crystal macrostructure occurred as the G/V ratio decreased below approximately 320 (K/mm / mm/sec). The transition to columnar crystals occurred when the G/V ratio dropped below 75.
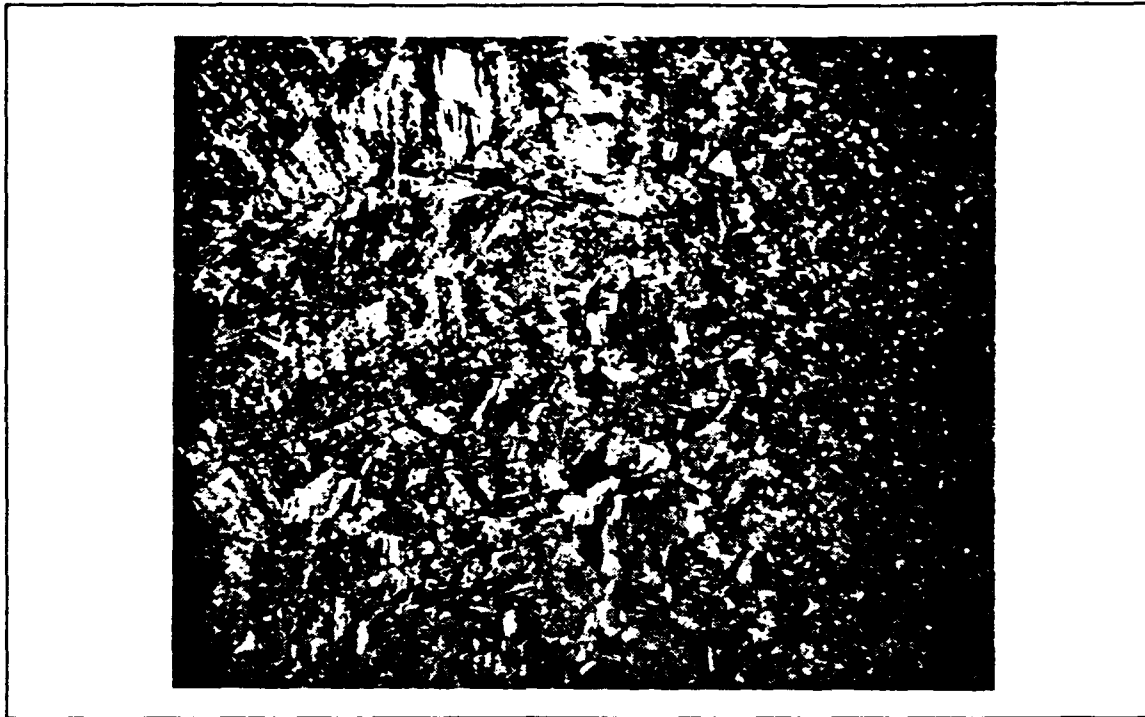
Figure 35 Photomicrograph. Weldment 4 top surface fusion line. 50X.

2. Substructure

The region where the solidification mode generally ceased to be planar and became cellular, columnar, or dendritic was conspicuous. This transition coincided with the transition from a planar to equiaxed macrostructure.

Assessing the substructure of the welds beyond this proved to be considerably more difficult than determining the macrostructure. In some instances, a columnar dendritic type substructure was clearly observed and in others, a cellular substructure was evident. However, almost invariably there was evidence of cellular, columnar, and dendritic substructures in very close proximity. As shown in Figure 39, in one micrograph at 200X magnification, substructures which are ostensibly cellular, columnar, and dendritic are all present. This type of solidification behavior, with multiple modes coexisting at virtually one point makes it difficult to ascertain what the solidification mode was at a point where the solidification parameters were calculated. The calculated solidification parameters should be interpreted as the conditions which exist over a fairly
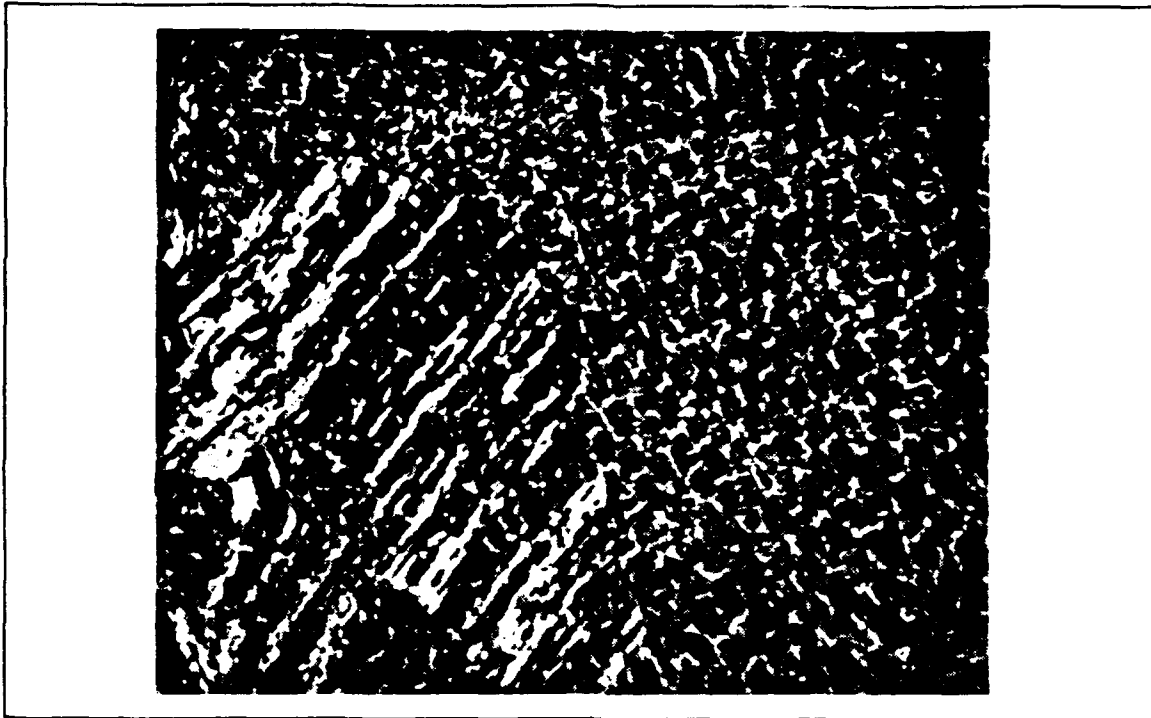
Figure 36 Photomicrograph. Weldment 1 transverse cross section. 200X.

broad region rather than a micro-condition. To present results indicating a successful categorization of the solidification mode at each point as in the case of macrostructure would be a gross oversimplification of the true physical situation.

Two distinct explanations are proposed. The most simplistic is that each of the modes which appears to exist really does. As in Figure 39, cellular, columnar, and dendritic structures are coexisting in the small area. Second, the entire region is dendritic, and the regions which look columnar and cellular are actually the ends of dendrites which were truncated during sectioning. When solidification occurs, it tends to be along the preferred growth directions. These [100] directions will be at different angles to the transverse section under observation. It is plausible that while solidification is purely dendritic, a cut made normal to the growth direction would appear to be cellular or columnar.

The first argument seems unlikely because it is known that the growth direction changes- a fact which has been studied in contrast to welds on single crystal

65
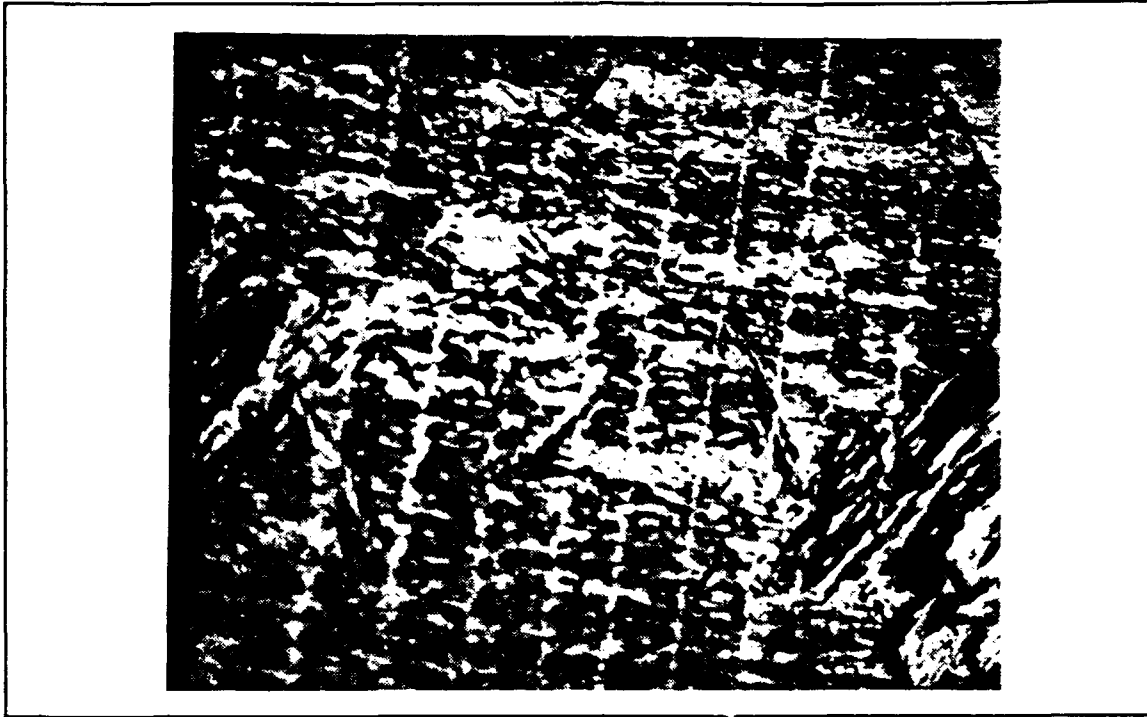
Figure 37 Photomicrograph. Weldment 1 top surface near weld centerline. 500X.

materials [Ref.24,25,26]. It follows that the angle between the growth direction and the plane of view changes when the growth direction shifts. The second explanation could be argued but would be very difficult to prove. The most realistic explanation, however, is combination of these two explanations. The notion that the growth direction changes supports the hypothesis that the velocity and solidification mode will change as well. When the direction changes, the orientation of growth velocity with temperature gradient will change and the magnitude of velocity will be affected. With new temperature gradient and crystal growth velocity, the solidification mode inevitably will change.

3. Relevance of Correlation

The quantified GV plot has some important uses. First, it provides insight into the solidification behavior of the weld. At a glance, one can ascertain how much the solidification parameters vary and the extent of their influence on the solidification morphology. Second, further development would allow the use of such a plot for weld

66
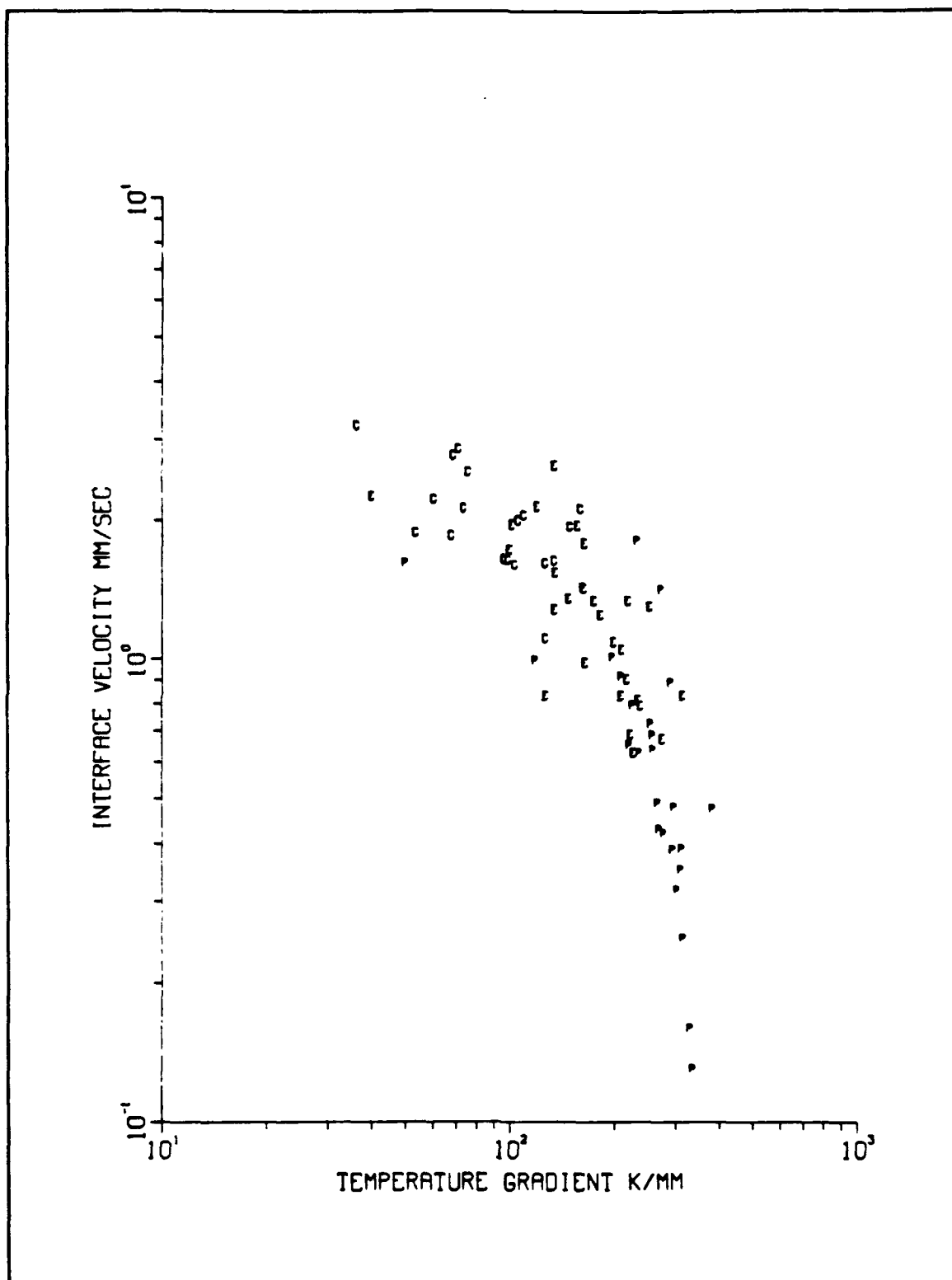
Figure 38 GV Plot for all data collected. 'P'= Planar; 'E'= Equiaxed crystals; and 'C'= Columnar crystals.
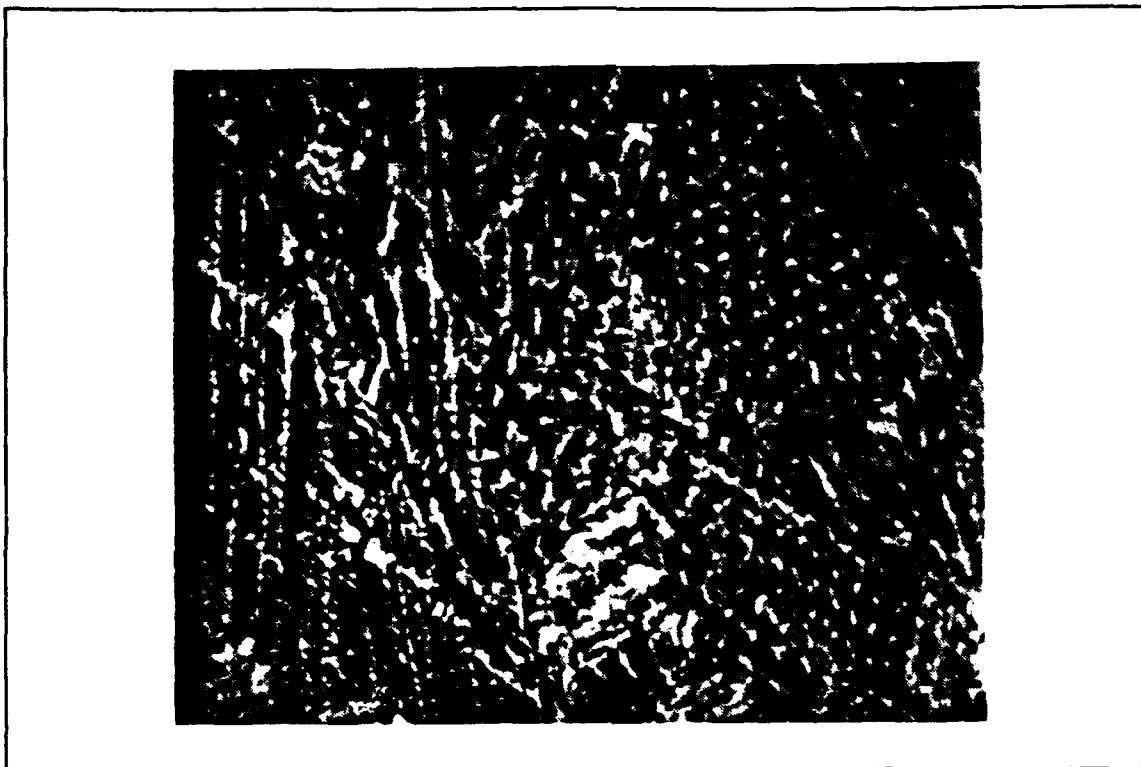
Figure 39 Photomicrograph. Region where multiple solidification modes ostensibly coexist. 200X.

solidification morphology prediction. As it stands now, the model must be adjusted at each run based on weld cross sections observed using optical microscopy techniques. At that point, the morphology can be viewed directly. However, through an innovation in the model, the heat input configuration could be determined as a function of the power variables. Then, the model would directly calculate the temperature field which leads to the solidification parameters with which the macrostructure would be predicted. Third, the calculated solidification parameters could be used for further modelling of the welding phenomenon. Presently, models are being developed which predict features of weld metallurgy based on the solidification parameters (discussed in Chapter II, Section B, Subsection 3) but are not applied to actual welds because the solidification parameters are not known. This important step in quantifying the solidification parameters has been illustrated here.

V. CONCLUSIONS AND RECOMMENDATIONS

The solidification parameters temperature gradient G and crystal growth velocity V were calculated based on the temperature field predicted by a numerical model. Solidification macrostructure was correlated with the solidification parameters and the results were encouraging. Presented in a GV type plot, the conditions which lead to planar growth, equiaxed crystals, and columnar crystals were reasonably distinct.

The correlation of the solidification substructure (solidification mode) with the solidification parameters was largely incomplete. The calculated solidification parameters are mean values. However, based on observations of multiple solidification modes in proximity, the conditions at the solid-liquid interface appear to have significant fluctuations. These apparent fluctuations in conditions at the solid-liquid interface are not quantified.

For further studies, it is recommended that additional model validation be accomplished first. The predicted size of the free surface of the weld pool could be compared with the observed surface sizes using a laser vision system. Also, embedded thermocouples placed outside the weld pool may be used to validate more time temperature curves.

As confidence in the accuracy of the model is increased, a second area for improvement is a refinement of the calculations of the solidification parameters. Most importantly, in the Taylor series expansion which lead to calculations of temperature gradients, the second order and higher order terms were neglected. The second order terms could be included. Also, solidification parameters were calculated only at discrete (X,Y) values. By making calculations at additional points on the solid-liquid interface, a much larger database could be constructed for correlations with substructure.

Finally, the methods employed in this study should be used again for other materials, and for studies of transient weld conditions.

APPENDIX I

Table 4 through Table 7 provide a complete summary of input and output data for weldments one through five, respectively. For the location of the points listed in the computed results, refer to the GV Plots, Figure 22 through Figure 25 in Chapter IV, section B.

TABLE 4 OUTPUT TABLE FOR WELDMENT ONE.

WELD SIMULATION DATA - RUN 1

FINISHING TIME: 15.0000 SECONDS

HEAT INPUT DATA
```
    VOLTAGE    :       14.4 VOLTS
    CURRE T    :       250. AMPS
    EFFICIENCY:       0.70 PERCENT
    ARC VEL    :       3.27 MM/SEC
    HEAT INPUT:     770.64 JOULES/MM   (EFFxAMPSxVOLTS/VEL)
    HEAT INPUT:    1100.92 JOULES/MM   (AMPSxVOLTS/VEL)
```

HEAT SOURCE CONFIGURATION
```
    A1    : 8.00
    B1    : 3.10
    C1    : 3.01
```

HEAT TRANSFER PROPERTIES
```
    SIGMA : 0.567E-07
    EPSIL :       0.820
    RHO   :      7890.0
    CPSP  :       536.0
```

RESULTS PREDICTED BY MODEL

VOLUME OF POOL: 143.24 CUBIC MM

N	I MM	J MM	DEPTH MM	GRAD K/MM	VEL MM/S	CR K/S	G/V	N
1	9	18	0.42	262.	0.42	110.14	622.	1
2	10	18	1.86	283.	0.87	246.70	324.	2
3	10	17	1.35	246.	1.28	314.24	193.	3
4	10	16	0.59	145.	1.91	277.28	76.	4
5	11	18	2.38	373.	0.47	173.82	800.	5
6	11	17	2.19	305.	0.82	250.40	373.	6
7	11	16	1.96	156.	2.08	324.82	75.	7
8	11	15	1.08	124.	1.59	196.62	78.	8
9	12	17	2.59	266.	1.39	369.72	191.	9
10	12	16	2.27	213.	1.32	280.55	162.	10
11	12	15	2.00	204.	0.82	166.52	249.	11
12	12	14	1.11	72.	2.09	150.41	34.	12
13	13	17	2.94	226.	1.78	402.25	127.	13
14	13	16	2.68	160.	1.76	281.19	91.	14
15	13	15	2.15	170.	1.32	223.74	129.	15
16	13	14	1.70	67.	2.73	182.89	25.	16
17	13	13	0.65	35.	3.16	112.12	11.	17
18	14	17	3.01	321.	0.16	50.27	2055.	18
19	14	16	2.82	153.	1.92	293.0	80.	19
20	14	15	2.23	159.	1.40	223.5	114.	20
21	14	14	1.89	69.	2.82	195.7	25.	21
22	14	13	1.04	52.	1.85	96.6	28.	22
23	15	17	2.94	226.	1.78	402.0	127.	23
24	15	16	2.68	160.	1.76	281.29	91.	24
25	15	15	2.15	170.	1.32	223.51	129.	25
26	15	14	1.71	67.	2.73	182.95	25.	26
27	15	13	0.67	35.	3.16	112.07	11.	27
28	16	17	2.59	265.	1.39	369.43	190.	28
29	16	16	2.27	213.	1.32	280.89	161.	29
30	16	15	2.01	203.	0.82	166.77	247.	30
31	16	14	1.12	72.	2.10	150.75	34.	31
32	17	18	2.38	372.	0.47	173.85	795.	32
33	17	17	2.20	305.	0.82	248.68	373.	33
34	17	16	1.97	156.	2.08	324.79	75.	34
35	17	15	1.09	122.	1.60	195.02	76.	35
36	18	17	1.36	245.	1.26	309.30	194.	36
37	18	16	0.63	145.	1.90	275.38	77.	37
38	19	18	0.44	261.	0.42	109.71	619.	38

TABLE 5 OUTPUT TABLE FOR WELDMENT TWO.

```
WELD SIMULATION DATA - RUN 2

FINISHING TIME:    15.0000   SECONDS

HEAT INPUT DATA
   VOLTAGE   :      14.5 VOLTS
   CURRENT   :      250. AMPS
   EFFICIENCY:      0.70 PERCENT
   ARC VEL   :      2.27 MM/SEC
   HEAT INPUT:   1117.84 JOULES/MM   (EFF×AMPS×VOLTS/VEL)
   HEAT INPUT:   1596.92 JOULES/MM   (AMPS×VOLTS/VEL)

HEAT SOURCE CONFIGURATION
   A1     :  9.01
   B1     :  3.10
   C1     :  3.80

HEAT TRANSFER PROPERTIES
   SIGMA : 0.567E-07
   EPSIL :      0.820
   RHO   :    7890.0
   CPSP  :     536.0


RESULTS PREDICTED BY MODEL

   VOLUME OF POOL:   195.11 CUBIC MM
```

N	I MM	J MM	DEPTH MM	GRAD K/MM	VEL MM/S	CR K/S	G/V	N
1	9	18	1.57	230.	0.62	141.28	373.	1
2	9	17	1.00	211.	0.89	187.82	237.	2
3	10	18	2.46	269.	0.41	110.92	654.	3
4	10	17	2.15	228.	0.80	182.59	284.	4
5	10	16	1.56	131.	1.26	165.03	104.	5
6	11	18	3.06	327.	0.13	41.62	2565.	6
7	11	17	2.89	178.	1.22	217.44	145.	7
8	11	16	2.30	161.	0.97	154.99	166.	8
9	11	15	1.76	94.	1.62	151.94	58.	9
10	12	18	3.31	307.	0.24	74.99	1258.	10
11	12	17	3.16	260.	0.48	124.60	542.	11
12	12	16	2.96	132.	1.52	200.58	87.	12
13	12	15	2.23	124.	1.09	134.81	113.	13
14	12	14	1.43	66.	1.83	120.80	36.	14
15	13	18	3.49	303.	0.34	104.11	880.	15
16	13	17	3.32	252.	0.62	156.90	403.	16
17	13	16	3.08	221.	0.62	135.85	359.	17
18	13	15	2.68	97.	1.62	156.43	60.	18
19	13	14	2.01	123.	0.82	101.15	151.	19
20	13	13	0.59	39.	2.22	86.90	18.	20
21	14	18	3.55	303.	0.38	115.75	796.	21
22	14	17	3.38	251.	0.67	168.32	374.	22
23	14	16	3.13	217.	0.67	146.56	322.	23
24	14	15	2.81	97.	1.70	166.00	57.	24
25	14	14	2.03	115.	0.98	112.27	118.	25
26	14	13	1.04	49.	1.59	77.66	31.	26
27	15	18	3.49	302.	0.35	104.80	873.	27
28	15	17	3.32	251.	0.63	157.26	401.	28
29	15	16	3.08	220.	0.62	135.97	357.	29
30	15	15	2.69	96.	1.63	156.47	59.	30
31	15	14	2.01	123.	0.83	101.63	148.	31
32	15	13	0.64	39.	2.23	87.67	18.	32
33	16	18	3.32	306.	0.25	76.30	1231.	33
34	16	17	3.16	259.	0.48	125.46	534.	34
35	16	16	2.97	132.	1.52	200.58	87.	35
36	16	15	2.25	121.	1.11	133.90	109.	36
37	16	14	1.47	66.	1.84	120.80	36.	37
38	17	18	3.07	325.	0.13	42.41	2497.	38
39	17	17	2.90	177.	1.23	217.18	144.	39
40	17	16	2.32	159.	0.97	154.45	163.	40
41	17	15	1.80	94.	1.63	152.39	57.	41

TABLE 6 OUTPUT TABLE FOR WELDMENT FOUR.

```
WELD SIMULATION DATA - RUN 4

FINISHING TIME:   15.0000  SECONDS

HEAT INPUT DATA
   VOLTAGE   :      13.0 VOLTS
   CURRENT   :      200. AMPS
   EFFICIENCY:      0.75 PERCENT
   ARC VEL   :      2.22 MM/SEC
   HEAT INPUT:    878.38 JOULES/MM   (EFFxAMPSxVOLTS/VEL)
   HEAT INPUT:   1171.17 JOULES/MM   (AMPSxVOLTS/VEL)

HEAT SOURCE CONFIGURATION
   A1    :  8.50
   B1    :  3.10
   C1    :  4.00

HEAT TRANSFER PROPERTIES
   SIGMA :  0.567E-07
   EPSIL :     0.820
   RHO   :    7890.0
   CPSP  :     536.0


RESULTS PREDICTED BY MODEL

   VOLUME OF POOL:   98.08 CUBIC MM
```

N	I MM	J MM	DEPTH MM	GRAD K/MM	VEL MM/S	CR K/S	G/V	N
1	10	17	1.11	220.	0.78	170.59	283.	1
2	11	17	2.08	289.	0.47	136.45	611.	2
3	11	16	1.46	144.	1.33	190.92	108.	3
4	12	17	2.43	248.	0.71	175.54	349.	4
5	12	16	2.08	232.	0.78	179.92	299.	5
6	12	15	1.26	101.	1.58	159.37	64.	6
7	13	17	2.78	203.	0.90	182.80	224.	7
8	13	16	2.27	205.	1.03	211.52	199.	8
9	13	15	1.77	99.	1.93	190.94	51.	9
10	14	17	2.89	192.	0.99	190.69	193.	10
11	14	16	2.35	194.	1.07	207.94	182.	11
12	14	15	1.93	103.	1.97	201.65	52.	12
13	14	14	0.31	59.	2.19	130.22	27.	13
14	15	17	2.78	202.	0.91	183.18	222.	14
15	15	16	2.27	204.	1.03	210.79	198.	15
16	15	15	1.78	99.	1.93	191.22	51.	16
17	16	17	2.43	246.	0.71	176.13	345.	17
18	16	16	2.08	230.	0.79	181.17	293.	18
19	16	15	1.27	100.	1.60	160.53	63.	19
20	17	17	2.09	287.	0.48	137.70	598.	20
21	17	16	1.48	143.	1.34	191.30	107.	21
22	18	17	1.14	219.	0.77	168.04	285.	22

TABLE 7 OUTPUT TABLE FOR WELDMENT FIVE.

```
WELD SIMULATION DATA - RUN 5

FINISHING TIME:    15.0000  SECONDS

HEAT INPUT DATA
    VOLTAGE   :       12.6 VOLTS
    CURRENT   :       200. AMPS
    EFFICIENCY:       0.75 PERCENT
    ARC VEL   :       3.27 MM/SEC
    HEAT INPUT:     577.98 JOULES/MM   (EFFxAMPSxVOLTS/VEL)
    HEAT INPUT:     770.64 JOULES/MM   (AMPSxVOLTS/VEL)

HEAT SOURCE CONFIGURATION
    A1    :  8.50
    B1    :  3.10
    C1    :  4.00

HEAT TRANSFER PROPERTIES
    SIGMA : 0.567E-07
    EPSIL :     0.820
    RHO   :    7890.0
    CPSP  :     536.0


RESULTS PREDICTED BY MODEL

VOLUME OF POOL:    48.50 CUBIC MM
```

N	I MM	J MM	DEPTH MM	GRAD K/MM	VEL MM/S	CR K/S	G/V	N
1	11	18	1.20	215.	0.64	136.35	338.	1
2	11	17	0.05	117.	2.11	247.22	56.	2
3	12	18	1.96	158.	1.41	223.24	112.	3
4	12	17	1.27	159.	1.68	267.24	94.	4
5	12	16	0.06	74.	2.51	186.48	30.	5
6	13	18	2.13	295.	0.31	92.22	945.	6
7	13	17	1.87	131.	2.59	339.64	50.	7
8	13	16	1.03	131.	1.61	210.85	82.	8
9	14	18	2.19	286.	0.38	108.68	751.	9
10	14	17	2.00	268.	0.66	178.18	404.	10
11	14	16	1.17	107.	2.02	215.72	53.	11
12	15	18	2.13	295.	0.31	92.14	944.	12
13	15	17	1.88	131.	2.59	339.57	50.	13
14	15	16	1.03	131.	1.61	211.34	81.	14
15	16	18	1.96	158.	1.41	222.96	112.	15
16	16	17	1.27	158.	1.69	266.85	93.	16
17	16	16	0.07	74.	2.52	187.02	29.	17
18	17	18	1.21	214.	0.64	136.20	336.	18
19	17	17	0.06	117.	2.11	247.14	56.	19

The source codes used extensively for the calculations and graphics in this thesis are provided here: PLOTHAZ FORTRAN and GVPLOT FORTRAN. PLOTHAZ FORTRAN was used for Figure 16, Figure 17, and Figure 18. GVPLOT FORTRAN was used for Figure 22 through Figure 25.

A. PLOTHAZ FORTRAN

```
C  THIS PROGRAM USES THE TEMPERATURE DATA PRODUCED BY THE
START
C  PROGRAMS AND MEASURED DATA TO PLOT BOTH THE PREDICTED AND
MEASURED
C  FUSION AND HEAT AFFECTED ZONE CROSS SECTIONS. GRAPHICS ARE
DONE WITH
C  DISSPLA. THE INPUT DATA FILE IS "FINAL FINAL", WHICH IS CREATED
BY
C  THE START PROGRAMS.
C  IT ALSO USES DATA FROM A FILE CALLED 'POOLCOMP DATA A', WHICH
C  IS DATA DESCRIBING THE MEASURED WELDPOOL GEOMETRY. THIS FILE
IS
C  CREATED BY THE USER IN THE FOLLOWING FORMAT:
C    NUMPOOL  NUMHAZ
C    XPOOL(0)       ZPOOL(0)
C    ...         ...
C    XPOOL(NUMPOOL) ZPOOL(NUMPOOL)
C    XHAZ(0)        ZHAZ(0)
C    ...         ...
C    XHAZ(NUMHAZ)   ZHAZ(NUMHAZ)
C
C  THE SCALE IS SET UP IN 'CALL AREA2D' AND 'CALL GRAF'.
C  THE FOLLOWING WILL PROVIDE A PLOT WITH MAGNIFICATION OF
C  5X :
C       CALL UNITS('MM')  SETS SUBSEQUENT UNITS TO MM
C       CALL AREA2D(135,40)  SETS THE PLOT SIZE TO 135X40 MM
C       CALL GRAF(1,2,27,7,-1,0)  PRESCRIBES APPROPRIATE AXES.
C
```

```
C ****IMPORTANT*****************************************
C * ANY OF THESE SETTINGS CAN BE CHANGED BUT MUST BE KEPT IN *
C * AGREEMENT OR THE PLOT WILL BE OUT OF SCALE.          *
C ***************************************************
C
      PROGRAM PLOTHAZ
      DIMENSION TEMP(27,8)
      DIMENSION TEMPIMP(2)
      DIMENSION XPOOL(50),ZPOOL(50),XHAZ(50),ZHAZ(50)
C
C  THE IMPORTANT TEMPERATURES FOR HY-80 STEEL ARE:
      TMELT=1770.0
      THAZ=1200.00
C
C  XCOR IS USED TO CORRECT THE HORIZONTAL ALLIGNMENT OF THE
MEASURED
C  WELD POOL. IE, TO MOVE THE MEASURED LINE OF SYMMETRY ONTO
THE
C  COMPUTED LINE OF SYMMETRY.
      XCOR=-0.2
C
C  THE FOLLOWING PRESCRIBE THE PERCENT OF RANGE VALUES THAT
ARE
C  PLOTTED. IE, 0%=MIN VALUE, 100%=MAX VALUE IN THE RANGE.
      TEMPIMP(1)=0.0
      TEMPIMP(2)=100.0
      CALL EXCMS('FILEDEF 1 DISK MAP DATA A')
      CALL EXCMS('FILEDEF 2 DISK POOLCOMP DATA A')
C
C  READ IN THE DATA FROM MAP:
      DO 100 K=8,1,-1
        READ(1,*) (TEMP(I,K),I=1,27)
  100 CONTINUE
C
C  READ IN THE DATA FROM POOLCOMP:
      READ(2,*) NUMPOOL,NUMHAZ
      DO 200 I=1,NUMPOOL
        READ(2,*) XPOOL(I),ZPOOL(I)
        ZPOOL(I)=8.0-ZPOOL(I)
        XPOOL(I)=XPOOL(I)+XCOR
  200 CONTINUE
      DO 300 I=1,NUMHAZ
        READ(2,*) XHAZ(I),ZHAZ(I)
```

76

```
      ZHAZ(I)=8.0-ZHAZ(I)
      XHAZ(I)=XHAZ(I)+XCOR
  300 CONTINUE
C
C
C  PLOT THE CONTOURS:
      CALL COMPRS
C
C  ESTABLISH THE PAGE SIZE, IN INCHES FOR NOW:
      CALL PAGE(11.0,8.5)
C
C  NOW SWITCH TO MILLIMETERS:
      CALL UNITS('MM')
C
C  THE AREA OF THE GRAPH ITSELF (MUST FIT ON THE PAGE):
      CALL AREA2D(130,35)
C
C
C  ANNOTATE- AXES AND TITLE:
      CALL XNAME('X (MM)',6)
      CALL YNAME('DEPTH (MM)',10)
C     CALL HEADIN('K IN POOL = 250.0',100,1,1)
C
C     PRESCRIBE  THE  UNITS  ON  THE  AXES.  IT  IS  IMPORTANT  (!!)  TO
REMEMBER
C  THAT THE SOFTWARE DOES NOT ASSUME ONE UNIT OF GRID IN YOUR
DATA IS
C  ONE UNIT OF LENGTH ON THE AXES. BE CAREFUL OR YOUR PLOT WILL
C  BE OUT OF SCALE!!
      CALL GRAF(1,2,27,7,-2,0)
C
C  PUT A FRAME ON THE PAGE
      CALL FRAME
C
C  SET WHICH CONTOURS ARE TO BE PLOTTED
      CALL CONLVS(TEMPIMP,2,'PERCENT')
C
C  SET THE RANGE
      CALL ZRANGE(THAZ,TMELT)
C
C  CREATE THE CONTOURS AND PLOT THEM.
      CALL CONMAK(TEMP,27,8,100)
      CALL CONTUR(2,'LABELS','DRAW')
```

```
C
C  GRIDS, IF DESIRED:
C     CALL GRID(2,2)
C
C  PLOT CONTOURS TO FIND THE EFFECTIVE HAZ TEMPERATURE
C     CALL ZRANGE(1200.,1500.)
C     CALL CONMAK(TEMP,27,8,100)
C     CALL CONTUR(3,'LABELS','DRAW')
C
C  END THE CONTOUR PLOTTING PART OF THE GRAPHICS
      CALL ENDGR(1)
C
C  NOW SET EVERYTHING UP AGAIN AND PLOT THE MEASURED POOL AND
HAZ
      CALL PAGE(11.0,8.5)
      CALL UNITS('MM')
      CALL AREA2D(130,35)
      CALL GRAF(1,2,27,7,-2,0)
C
C  MAKE THE WELDPOOL A DOTTED LINE
      CALL DOT
      CALL CURVE(XPOOL,ZPOOL,NUMPOOL,0)
C
C  AND THE HAZ A DASHED LINE
      CALL DASH
      CALL CURVE(XHAZ,ZHAZ,NUMHAZ,0)
C
C  END THE PLOTTING ROUTINE
      CALL DONEPL
      END
```

B. GVPLOT FORTRAN

```
C
C PROGRAM GVPLOT FINDS THE SOLID-LIQUID INTERFACE OF THE FUSION
C ZONE IN A WELD SIMULATED BY THE START PROGRAM. THEN THE
DIRECTIONAL
C    DERIVATIVES OF TEMPERATURE ARE CALCULATED AT THE
SOLID-LIQUID
C INTERFACE. USING THE DIRECTIONAL DERIVATIVE OF TEMPERATURE,
THE
C TEMPERATURE GRADIENT AND CRYSTAL GROWTH VELOCITY ARE
CALCULATED.
C ALL OF THE RESULTS ARE PRESENTED GRAPHICALLY. AN INDEX IS
ASSIGNED
C TO EACH POINT WHERE THE GRADIENT AND GROWTH VELOCITY ARE
CALCULATED.
C THE INDEX IS PRINTED ON A CROSS SECTION OF THE FUSION ZONE. A
GV
C PAIR CALCULATED AT (X,Y,Z) IS PLOTTED AT (X,Z) ON THE CROSS
SECTION.
C THEN THE INDEX NUMBER IS PLOTTED ON A GV TYPE PLOT: A LOG-LOG
PLOT
C WITH TEMPERATURE GRADIENT ON THE X AXIS AND CRYSTAL GROWTH
VELOCITY
C ON THE Y AXIS.
C THE ONLY FILE WHICH IS REQUIRED BY THIS PROGRAM IS "FILE FINAL"
C WHICH IS AN OUTPUT FILE CREATED BY THE START PROGRAMS.
C
C
      PROGRAM GVPLOT
C
      DIMENSION TEMP(27,27,8),ZMELT(27,27),GRAD(27,27),V(27,27)
      DIMENSION TMAP(27,8),TMAP2(17,5),TEMPIMP(5)
      DIMENSION XGV(100),YGV(100)
C
C OPEN THE INPUT FILE
      OPEN(1,FILE='FINAL',STATUS='OLD',FORM='UNFORMATTED')
C
C INITIALIZE THE ARRAYS
      DATA ZMELT / 729*8.0 /
      DATA GRAD /729*0./
      DATA TMAP /216*0.0/
      TMELT=1770.0
```

```fortran
      READ(1) TIME
      READ(1) (((TEMP(I,J,K),I=1,27),J=1,27),K=1,8)
      READ(1) VTORCH
C
C
C ACQUIRE A MAP OF MAX TEMPERATURES IN (X,Z) IN ORDER TO DEFINE
THE
C FUSION ZONE
      DO 300 I=1,27
      DO 300 J=1,27
      DO 300 K=1,8
        IF (TEMP(I,J,K).GT.TMAP(I,9-K)) TMAP(I,9-K)=TEMP(I,J,K)
 300  CONTINUE
C
C
C FIND THE SOLID-LIQUID INTERFACE BY SEARCHING THE TEMPERATURE
FIELD
C AND INTERPOLATING
      DO 100 I=1,27
      DO 100 J=1,27
        DO 110 K=1,7
         IF (TEMP(I,J,K).GT.TMELT.AND.TEMP(I,J,K+1).LT.TMELT) THEN
           ZMELT(I,J)= 9 - (TEMP(I,J,K)-TMELT)
     *        /(TEMP(I,J,K)-TEMP(I,J,K+1)) - K
         ENDIF
 110    CONTINUE
 100  CONTINUE
C
C
C
C
C TRUNCATE SOME OF THE DATA TO ENLARGE THE DISPLAYED POOL SIZE
      DO 102 K=1,5
      DO 102 I=1,17
        TMAP2(I,K) = TMAP(I+5,K+3)
 102  CONTINUE
C
C PLOT THE FUSION ZONE
      CALL COMPRS
      CALL PAGE(8.5,11.0)
      CALL PHYSOR(1.5,7.9)
      CALL AREA2D(5.5,1.375)
      CALL XNAME('X MM',6)
```

```
          CALL YNAME('Z MM',6)
          CALL HEADIN('INDEX OF CALCULATED POINTS',45,2,1)
          CALL GRAF(6,2,22,4,-2,0)
          CALL FRAME
          CALL CONLVS(TEMPIMP,1,'PERCENT')
          CALL ZRANGE(THAZ,TMELT)
          CALL CONMAK(TMAP2,17,5,100)
          CALL CONTUR(1,'LABELS','DRAW')
C
C
C STARTING FORWARD OF THE WELD POOL WORK TOWARDS THE AFT
AND FIND WHERE
C THE CURVE OF THE INTERFACE BEGINS TO SLOPE UP, IE WHERE IS IT IS
C SOLIDIFYING INSTEAD OF MELTING.
C THEN, FIND THE NORMAL DERIVATIVE (GRADIENT OF AN ISOTHERM) BY
DOING
C A TAYLOR SERIES EXPANSION ABOUT THE POINT.
C
          NUM=0
          NLAST=0
          DO 200 I=1,27
          DO 200 J=26,1,-1
            IF (ZMELT(I,J).LT.7.99) THEN
C         (I,J) CORRESPONDS TO THE FUSION ZONE AREA
              IF (ZMELT(I,J).GT.ZMELT(I,J+1))THEN
C           NOT MELTING, BUT SOLIDIFYING
                IZSTAR=8-INT(ZMELT(I,J))
                DELTAZ=INT(ZMELT(I,J))+1-ZMELT(I,J)
                TSUBZ=(TEMP(I,J,IZSTAR)-TMELT)/(DELTAZ)
                TSUBY=TEMP(I,J+1,IZSTAR)-TMELT-TSUBZ*DELTAZ
                TSUBX=0.0
                IF (I.GT.14) THEN
                  TSUBX=TEMP(I-1,J+1,IZSTAR)-TMELT-TSUBY
     *             -TSUBZ*DELTAZ
                ELSEIF (I.LT.14) THEN
                  TSUBX=TEMP(I+1,J+1,IZSTAR)-TMELT-TSUBY
     *             -TSUBZ*DELTAZ
                ENDIF
                GRAD(I,ZMELT(I,J))=SQRT(TSUBX*TSUBX+TSUBY*TSUBY
     *             +TSUBZ*TSUBZ)
C
                V(I,ZMELT(I,J))=(TSUBY/GRAD(I,ZMELT(I,J)))*VTORCH
C
```

81

```fortran
                  NUM=NUM+1
                  IF (I.LE.14) NLAST=NLAST+1
                  XGV(NUM)=GRAD(I,ZMELT(I,J))
                  YGV(NUM)=V(I,ZMELT(I,J))
C
C
C         PLOT THE INDEX NUMBER ON THE FUSION ZONE CROSS SECTION
                  CALL HEIGHT(0.08)
                  CALL RLINT(NUM,I,8-ZMELT(I,J))
              ENDIF
          ENDIF
  200  CONTINUE
C
C
C
C  NOW SET UP THE GVPLOT
       CALL ENDGR(1)
       CALL OREL(0.7,-6.20)
       CALL AREA2D(4.0,4.2)
       CALL RESET('HEIGHT')
       CALL XNAME('TEMPERATURE GRADIENT K/MM',30)
       CALL YNAME('INTERFACE VELOCITY MM/SEC',30)
       CALL LOGLOG(10.,2.00,0.1,1.4)
       CALL HEADIN('GV PLOT',45,2,1)
       CALL HEIGHT(0.065)
C
C     PUT THE INDEX NUMBER AT (G,V) ON THE GV PLOT
       DO 400 I=1,NLAST
          CALL RLINT(I,XGV(I),YGV(I))
C
  400  CONTINUE

       CALL DONEPL
       END
```

LIST OF REFERENCES

1. David, S.A., and Vitek, J.M., "Correlation between Solidification Parameters and Weld Macrostructures", *International Materials Review*, v.34, 1989.

2. Easterling, K., *Introduction to the Physical Metallurgy of Welding*, Butterworth, 1983.

3. Kuo, S., *Welding Metallurgy*, John Wiley & Sons, 1987.

4. Kraus, H.G., "Optical Spectral Radiometric Method for Measurement of Weld-pool Surface Temperatures," *Optics Letters*, v.11, No.12, December, 1986.

5. Kraus, H.G., "Experimental Measurement of Thin Plant 304 Stainless Steel GTA Weld Pool Surface Temperatures," *Welding Journal*, p353-s, December, 1987.

6. Alcini, W.V., "Measurement of Temperature and Potential Fields in Spot Welding," Ph.D. Dissertation, The University of Michigan, 1988.

7. General Electric Report 86SRD013, *Minor Element Effects on Gas Tungsten Arc Weld Penetration*, December, 1986.

8. Ule, R.L., "A Study of the Thermal Profiles During Autogenous Arc Welding," M.S. and M.E. Thesis, Naval Postgraduate School, Monterey, CA, March, 1989.

9. Sedy, E.B., "Validation of a Computational Model for Autogenous Arc Welding," M.S. and M.E. Thesis, Naval Postgraduate School, Monterey, CA, March, 1990.

10. Ule, R.L., Joshi, Y., and Sedy, E.B., "A New Technique for Three-Dimensional Transient Heat Transfer Computations of Autogenous Arc Welding," *Metallurgical Transactions B*, v.21B, December, 1990.

11. Rosenthal, D., "The Theory of Moving Sources of Heat and its Application to Metal Treatments," *Transactions ASME*, v.68, November, 1946.

12. Kurz, W., and Fisher, D.J., *Fundamentals of Solidification*, Trans Tech Publications, 1986.

13. Trivedi, R., and Kurz, W., "Morphological Stability of a Planar Interface Under Rapid Solidification Conditions," *Acta Metallurgica*, v.34, No.5, 1986.

14. Kurz, W., Giovanola, B., and Trivedi, R., "Theory of Microstructural Development during Rapid Solidification," *Acta Metallurgica*, v.34, No.5, pp 823, 1986.

15. Trivedi, R., Sekhar, J.A., and Seetharaman, V., "Solidification Microstructures near the Limit of Absolute Stability," *Metallurgical Transactions A*, v.20A, April, 1989.

16. Fabrietti, L.M., and Trivedi, R., "Nonequilibrium Effects during the Ledgewise Growth of a Solid-Liquid Interface," *Metallurgical Transactions A*, v.22A, June, 1991.

17. Gruegel, R.N., and Zhou, Y., "Primary Dendrite Spacing and the Effect of Off-Axis Heat Flow," *Metallurgical Transactions A*, v.20A, May, 1989.

18. Rappaz, M., "Modelling of Microstructure Formation in Solidification Processes," *International Materials Review*, v.34, No.3, 1989.

19. Savage, W.F., Nippes, E.F., and Erickson, J.S., "Solidification Mechanisms in Fusion Welds," *Welding Journal*, p213-s, August, 1976.

20. Espinosa, D.C., "Visualization of Gas Tungsten Arc Welds," Naval Postgraduate School, Monterey, CA, September, 1991.

21. Xiao, Y.H., and den Ouden, G., "A Study of GTA Weld Pool Oscillation," *Welding Journal*, August, 1990.

22. Massalski, T., *Binary Alloy Phase Diagram*, ASM International, Second Edition, 1990.

23. Thermal conductivity and heat capacity data for HY-80 steel were provided by William Morris, David Taylor Research Center, Annapolis, Maryland. Source was United States Steel.

24. Rappaz, M., David, S.A., Vitek, and J.M., Boatner, L.A., "Development of Microstructure in Fe-15Ni-15Cr Single Crystal Electron Beam Welds," *Metallurgical Transactions A*, v.20A, June, 1989.

25. David, S.A., Vitek, J.M., Rappaz, M., and Boatner, L.A., "Microstructure of Stainless Steel Single-Crystal Electron Beam Welds," *Metallurgical Transactions A*, v.21A, June, 1990.

26. Rappaz, M., David, S.A., Vitek, and J.M., Boatner, L.A., "Analysis of Solidification Microstructure in Fe-Ni-Cr Single Crystal Welds," *Metallurgical Transactions A*, v.21A, June, 1990.

INITIAL DISTRIBUTION LIST

No. Copies

1. Defense Technical Information   2
   Cameron Station
   Alexandria, VA 22304-6145

2. Library, Code 52   2
   Naval Postgraduate School
   Monterey, CA 94943-5002

3. SEA-05   1
   Naval Sea Systems Command
   Washington, DC 20362-5101

4. SEA-92R   1
   Naval Sea Systems Command
   Washington, DC 20362-5101

5. Department Chairman, Code ME   1
   Department of Mechanical Engineering
   Naval Postgraduate School
   Monterey, CA 93940-5000

6. Richard Morris, Code 2815   1
   Annapolis Detachment, Carderock Division
   Naval Surface Warfare Center
   Annapolis, MD 21402-5067

7. Gene Franke, Code 2815   1
   Annapolis Detachment, Carderock Division
   Naval Surface Warfare Center
   Annapolis, MD 21402-5067

8. Mike Vassilaros, Code 2815   1
   Annapolis Detachment, Carderock Division
   Naval Surface Warfare Center
   Annapolis, MD 21402-5067

9. Alan G. Fox, Code MEFx   2
    Naval Postgraduate School
    Monterey, CA 93943-5000

10. Yogendra Joshi, Code MEYi   2
    Naval Postgraduate School
    Monterey, CA 93943-5000

11. Francis G. Novak   1
    33 Chateau Mouton
    Kenner, LA 70115

END

FILMED

DATE:
11-92

DTIC